The Astrophysical Journal Supplement Series, 273:14 (30pp), 2024 July https://doi.org/10.3847/1538-4365/ad3cd3

PHANGS-HST Catalogs for ∼100,000 Star Clusters and Compact Associations in 38 Galaxies. I. Observed Properties

Daniel Maschmann[1], Janice C. Lee[1,2,3], David A. Thilker[4], Bradley C. Whitmore[2], Sinan Deger[5,6], Médéric Boquien[7], Rupali Chandar[8], Daniel A. Dale[9], Aida Wofford[10,11], Stephen Hannon[12], Kirsten L. Larson[13], Adam K. Leroy[14], Eva Schinnerer[12], Erik Rosolowsky[15], Leonardo Úbeda[2], Ashley T. Barnes[16], Eric Emsellem[16,17], Kathryn Grasha[18,19,31], Brent Groves[20], Rémy Indebetouw[21,22], Hwihyun Kim[3], Ralf S. Klessen[23,24], Kathryn Kreckel[25], Rebecca C. Levy[1,32], Francesca Pinna[12,26,27], M. Jimena Rodríguez[1,28], Qiushi Tian[29], and Thomas G. Williams[30]

[1] Steward Observatory, University of Arizona, Tucson, AZ 85721, USA; danielmaschmann@arizona.edu
[2] Space Telescope Science Institute, 3700 San Martin Drive, Baltimore, MD 21218, USA
[3] Gemini Observatory/NSF's NOIRLab, 950 N. Cherry Avenue, Tucson, AZ 85719, USA
[4] Department of Physics and Astronomy, The Johns Hopkins University, Baltimore, MD 21218, USA
[5] Institute of Astronomy, University of Cambridge, Madingley Road, Cambridge CB3 0HA, UK
[6] Kavli Institute for Cosmology Cambridge, Madingley Road, Cambridge CB3 0HA, UK
[7] Université Côte d'Azur, Observatoire de la Côte d'Azur, CNRS, Laboratoire Lagrange, 06000, Nice, France
[8] University of Toledo, 2801 W. Bancroft Street, Mail Stop 111, Toledo, OH 43606, USA
[9] Department of Physics and Astronomy, University of Wyoming, Laramie, WY 82071, USA
[10] Instituto de Astronomía, Universidad Nacional Autónoma de México, Unidad Académica en Ensenada, Km 103 Carr. Tijuana-Ensenada, Ensenada, B.C., C.P. 22860, Mexico
[11] Department of Astronomy and Astrophysics, University of California, San Diego, 9500 Gilman Drive, La Jolla, CA 92093, USA
[12] Max-Planck-Institut für Astronomie, Königstuhl 17, D-69117, Heidelberg, Germany
[13] AURA for the European Space Agency (ESA), Space Telescope Science Institute, 3700 San Martin Drive, Baltimore, MD 21218, USA
[14] Department of Astronomy, The Ohio State University, 140 W. 18th Avenue, Columbus, OH 43210, USA
[15] Department of Physics, University of Alberta, Edmonton, AB T6G 2E1, Canada
[16] European Southern Observatory, Karl-Schwarzschild Straße 2, D-85748 Garching bei München, Germany
[17] Univ Lyon, Univ Lyon 1, ENS de Lyon, CNRS, Centre de Recherche Astrophysique de Lyon UMR5574, F-69230 Saint-Genis-Laval, France
[18] Research School of Astronomy and Astrophysics, Australian National University, Canberra, ACT 2611, Australia
[19] ARC Centre of Excellence for All Sky Astrophysics in 3 Dimensions (ASTRO 3D), Australia
[20] International Centre for Radio Astronomy Research, University of Western Australia, 35 Stirling Highway, Crawley, WA 6009, Australia
[21] University of Virginia Astronomy Department, 530 McCormick Road, Charlottesville, VA 22904, USA
[22] National Radio Astronomy Observatory, 520 Edgemont Road, Charlottesville, VA 22903-2475, USA
[23] Universität Heidelberg, Zentrum für Astronomie, Institut für Theoretische Astrophysik, Albert-Ueberle-Str 2, D-69120 Heidelberg, Germany
[24] Universität Heidelberg, Interdisziplinäres Zentrum für Wissenschaftliches Rechnen, Im Neuenheimer Feld 205, D-69120 Heidelberg, Germany
[25] Astronomisches Rechen-Institut, Zentrum für Astronomie der Universität Heidelberg, Mönchhofstraße 12-14, D-69120 Heidelberg, Germany
[26] Instituto de Astrofísica de Canarias, C/ Vía Láctea s/n, E-38205, La Laguna, Spain
[27] Departamento de Astrofísica, Universidad de La Laguna, Av. del Astrofísico Francisco Sánchez s/n, E-38206, La Laguna, Spain
[28] Instituto de Astrofísica de La Plata, CONICET–UNLP, Paseo del Bosque S/N, B1900FWA La Plata, Argentina
[29] Astronomy Department and Van Vleck Observatory, Wesleyan University, 96 Foss Hill Drive, Middletown, CT 06459, USA
[30] Sub-department of Astrophysics, Department of Physics, University of Oxford, Keble Road, Oxford OX1 3RH, UK

Received 2023 November 22; revised 2024 March 6; accepted 2024 March 17; published 2024 July 9

Abstract

We present the largest catalog to date of star clusters and compact associations in nearby galaxies. We have performed a *V*-band-selected census of clusters across the 38 spiral galaxies of the PHANGS–Hubble Space Telescope (HST) Treasury Survey, and measured integrated, aperture-corrected near-ultraviolet-*U*-*B*-*V*-*I* photometry. This work has resulted in uniform catalogs that contain ∼20,000 clusters and compact associations, which have passed human inspection and morphological classification, and a larger sample of ∼100,000 classified by neural network models. Here, we report on the observed properties of these samples, and demonstrate that tremendous insight can be gained from just the observed properties of clusters, even in the absence of their transformation into physical quantities. In particular, we show the utility of the UBVI color–color diagram, and the three principal features revealed by the PHANGS-HST cluster sample: the young cluster locus, the middle-age plume, and the old globular cluster clump. We present an atlas of maps of the 2D spatial distribution of clusters and compact associations in the context of the molecular clouds from PHANGS–Atacama Large Millimeter/submillimeter Array. We explore new ways of understanding this large data set in a multiscale context by bringing together once-separate techniques for the characterization of clusters (color–color diagrams and spatial distributions) and their parent galaxies (galaxy morphology and location relative to the galaxy main sequence).

---

[31] ARC DECRA Fellow.

[32] NSF Astronomy and Astrophysics Postdoctoral Fellow.

A companion paper presents the physical properties: ages, masses, and dust reddenings derived using improved spectral energy distribution fitting techniques.

Unified Astronomy Thesaurus concepts: Star formation (1569); Star clusters (1567); Galaxy evolution (594)

Supporting material: figure set, machine-readable tables

1. Introduction

Decades of research on star formation have taught us that systematic observations—spanning key spatial scales and phases of the star formation cycle, over a full set of galactic environments—are essential for development of a robust, unified model of star formation and galaxy evolution (e.g., Kennicutt & Evans 2012). To enable such an integrated multiphase, multiscale study of star formation, the Physics at High Angular resolution in Nearby GalaxieS (PHANGS) collaboration (Schinnerer et al. 2019) has conducted large surveys with Atacama Large Millimeter/submillimeter Array (ALMA; Leroy et al. 2021), Very Large Telescope (VLT)/MUSE (Emsellem et al. 2022), Hubble Space Telescope (HST; Lee et al. 2022), and JWST (Lee et al. 2023), and is studying the relationships between molecular clouds, H II regions, dust, and star clusters across the large diversity of environments found in nearby galaxies. Beyond these four principal surveys, a wealth of additional supporting data is available and continues to be obtained by PHANGS including Astrosat far-ultraviolet (FUV)/near-ultraviolet (NUV) imaging (PI: E. Rosolowsky; Hassani et al. 2024), HST Hα narrowband imaging (PIs: R. Chandar, D. Thilker, F. Belfiore), ground-based wide-field Hα narrowband imaging (PIs: G. Blanc, I.-T. Ho), and H I 21 cm observations with the Very Large Array and MeerKAT. To support the science analysis with this wealth of data, PHANGS has been producing and publicly releasing an extensive set of "higher level science products."[33]

In the context of this comprehensive effort, NUV-*U*-*B*-*V*-*I* imaging for 38 spiral galaxies was obtained from 2019 to 2021 through an HST Cycle 26 Treasury program. The galaxies were drawn from the PHANGS-ALMA parent sample and thus have ^{12}CO($J = 2 \rightarrow 1$) observations at $\sim 1''$ resolution. Half of the sample (19 galaxies) are covered by all four principal surveys of PHANGS; i.e., in addition to the HST and ALMA observations, integral field spectroscopic mapping from 4800 to 9300 Å has been performed with VLT/MUSE, and imaging in eight bands from 2 to 21 μm is being obtained through a JWST Cycle 1 Treasury program. Details on the design of the PHANGS-ALMA, PHANGS-HST, PHANGS-MUSE, and PHANGS-JWST foundational surveys are provided in the papers cited above. New large HST and JWST surveys to expand the number of galaxies with HST-JWST-ALMA data to 74 have been recently approved in 2023 (JWST Cycle 2, GO-3707, PI A. Leroy; HST Cycle 31, GO-17502, PI D. Thilker).

As discussed in Lee et al. (2022), one of the main goals of the PHANGS-HST Treasury Survey is to conduct a uniform census of star clusters and stellar associations in 38 nearby spiral galaxies ($d \lesssim 20$ Mpc) to probe cluster formation and evolution, and to utilize these effectively single-age stellar populations as "clocks" to time star formation and interstellar matter (ISM) processes. Here, we present the result of this census: catalogs providing the photometric properties of $\sim$100,000 star clusters and compact associations, the largest such sample to date. These catalogs are the culmination of technical efforts as summarized in Lee et al. (2022) to establish improved techniques for cluster candidate detection and selection (Whitmore et al. 2021; Thilker et al. 2022), photometry (Deger et al. 2022), and automated morphological classification using machine-learning (ML) techniques (Wei et al. 2020; Whitmore et al. 2021; Hannon et al. 2023).

A companion paper (Thilker et al. 2024, hereafter Paper II) presents the physical properties of the sample (specifically, age, mass, and reddening) derived using improved strategies for spectral energy distribution (SED) fitting, which were initially explored by Whitmore et al. (2023a). The improvements seek to mitigate the age–reddening–metallicity degeneracy by building upon conventional SED fitting techniques for star clusters, which were adopted at the outset of the PHANGS-HST survey (Turner et al. 2021). All of the catalogs described here can be accessed through the Mikulski Archive for Space Telescopes (MAST).[34]

The PHANGS-HST star cluster catalogs enable a wide range of science investigations. Many of the studies by the PHANGS team that have utilized these catalogs so far have focused on star formation feedback and timescales, but investigations of the old stellar populations (globular clusters) have also begun (Floyd et al. 2024). We briefly describe some of these studies below.

Barnes et al. (2022) examine the clusters and associations within isolated, compact H II regions in NGC 1672, identified through HST narrowband imaging. They find higher pressures (as measured from PHANGS-MUSE) within more compact H II regions, although with significant scatter, which is presumably introduced by variation in the stellar population properties (e.g., mass, age, metallicity).

By cross matching star clusters and multiscale stellar associations with H II regions from PHANGS-MUSE across the full set of 19 galaxies with PHANGS-HST+MUSE data, Scheuermann et al. (2023) study how H II regions evolve over time. They find that younger nebulae are more attenuated by dust and closer to giant molecular clouds, as expected by feedback-regulated models of star formation. They also report strong correlations with local metallicity variations and age, suggesting that star formation preferentially occurs in locations of locally enhanced metallicity.

Across this same set of 19 galaxies, Egorov et al. (2023) study the star clusters and associations within nebular regions of locally elevated velocity dispersion, including expanding superbubbles, identified with PHANGS-MUSE. They find that the kinetic energy of the ionized gas is correlated with the inferred mechanical energy input from supernovae (SNe) and stellar winds, which can be interpreted as a coupling efficiency of 10%–20%. They also find that young clusters and associations are preferentially located along the rims of superbubbles, which provides possible evidence for star formation propagation or triggering.

---

[33] https://sites.google.com/view/phangs/home/data

[34] https://archive.stsci.edu/hlsp/phangs/phangs-cat

Watkins et al. (2023b) perform a similar analysis, but starting with molecular gas superbubbles in PHANGS-ALMA. They measure radii and expansion velocities, and dynamically derive bubble ages and the mechanical power from young stars required to drive the bubbles. They find that the masses and ages of the PHANGS-HST clusters and associations are consistent with the required power, if an SN model that injects energy with a coupling efficiency of $\sim$10% is assumed.

A joint HST-JWST analysis with the IR imaging from the PHANGS-JWST Cycle 1 Treasury has also begun, and the first results have been published in a collection of papers for a PHANGS-JWST *Astrophysical Journal Letters* focus issue.[35]

One of the most striking features of the PHANGS-JWST MIRI imaging is the ubiquitous bubble structure (Lee et al. 2023; Williams et al. 2024). Watkins et al. (2023a) and Barnes et al. (2023) demonstrate star formation feedback are likely to be the origin of these bubbles, based on analysis of the PHANGS-HST star cluster and associations catalogs for NGC 628. Thilker et al. (2023) study the dust filament network in NGC 628 and its relation to sites of star formation, finding that >60% optically selected young clusters (<5 Myr) occurs within $\sim$25 pc dust filaments. Rodríguez et al. (2023) and Whitmore et al. (2023b) present first results on dust embedded star clusters, which trace the youngest sites of star formation, with the PHANGS-HST clusters and associations serving as a essential reference for computing constraints on the timescales for dust clearing and the embedded phase.

In this paper, we describe the PHANGS-HST catalogs of star clusters and compact associations with the aim of supporting further science with this extensive data set. The characterization of the observed properties presented in this paper provides a starting point for the utilization of the full census of star clusters and compact associations across the PHANGS-HST 38 galaxy sample to realize the aim of PHANGS to understand the interplay of the small-scale physics of gas and star formation with galactic structure and galaxy evolution.

The remainder of this paper is organized as follows. In Section 2, we provide an overview of the PHANGS-HST galaxy sample, HST observations, and star cluster and compact association catalog production pipeline, and describe the publicly released catalog structure and contents. In Section 3, we examine the size and photometric depths of the samples detected in each galaxy. In Section 4, we continue to develop the ideas introduced in J. Lee et al. (2024, in preparation) on using UV–optical color–color diagrams to gain insight into star cluster formation and evolution. We explore new ways of understanding the data in a multiscale context by studying the features of the UBVI star cluster color–color diagrams for each galaxy in relation to its position relative to the star-forming galaxy main sequence (MS) in star formation rate (SFR) and stellar mass (M_*). This composite diagram provides a framework for understanding cluster formation, evolution, and destruction in the context of the global properties of their host galaxies. In Section 6, we present an atlas of maps illustrating the 2D spatial distributions of the clusters and compact associations relative to giant molecular clouds from the PHANGS-ALMA CO(2-1) catalogs. We bring together characteristics of the cluster spatial distributions and color–color diagrams, with galaxy morphology and position along the MS to gain qualitative insight into the global drivers of cluster formation and evolution. In Section 9, we discuss issues related to sample completeness to outline future work and to provide advice to users of the catalog. Key conclusions are summarized in Section 10.

Vega magnitudes are used in this paper to facilitate a comparison to prior work.

2. Star Cluster Catalogs

As mentioned in the introduction, the PHANGS-HST catalogs of star clusters and compact associations are the end-product of an extensive processing pipeline. In this section, we provide a brief overview of the HST observations and this pipeline. The reader is referred to the corresponding technical papers, as cited in the Introduction and below, for a full discussion. Documentations of the PHANGS-HST imaging filters and exposure times for individual galaxies are provided in the next section as these are needed to understand the depth of the cluster catalogs.

2.1. Galaxy Sample and Observations

Galaxies for the PHANGS-ALMA parent sample were selected to be nearby ($D \lesssim 20$ Mpc), massive ($M_* \gtrsim 10^{9.75}\ M_\odot$), on the star-forming galaxy MS, and relatively face-on (Leroy et al. 2021). A subset of these were chosen for observation with HST (GO-15654) as discussed in Lee et al. (2022). The resulting PHANGS-HST sample is comprised of 38 spiral galaxies with morphological types of Sa through Sd, specific SFR (sSFR) from $\sim 10^{-10.5}$ to 10^{-9} yr^{-1}, SFR from $\sim$0.2 to 17 $M_\odot$ yr^{-1}, and molecular gas surface density ($\Sigma_{\rm mol}$) from $\sim 10^{0.5}$ to $10^{2.7}\ M_\odot$ pc^{-2} (see Lee et al. 2022; Table 1 and Figure 1).

PHANGS-HST imaging targeted the star-forming galaxy disk, and includes a combination of new and archival observations in five filters: F275W (NUV), F336W (*U*), F438W or F435W (*B*), F555W (*V*), and F814W (*I*).[36] We obtained new imaging of 34 galaxies with 43 WFC3 pointings using an allocation of 122 orbits. Archival NUV-*U*-*B*-*V*-*I* observations from the LEGUS survey (Calzetti et al. 2015)[37] were used for seven galaxies (NGC 0628, NGC 1433, NGC 1512, NGC 1566, NGC 3351, NGC 3627, NGC 6744; for the latter three, we obtained additional imaging to increase the HST footprint and match PHANGS-ALMA coverage of the disk). Suitable archival imaging in selected bands was available for 16 other galaxies.

Table 1 summarizes all HST observations, and specifies the cameras used and the exposure times. The new data obtained for PHANGS-HST and the archival data were processed together using the same data reduction pipeline (as summarized by Lee et al. 2022) to ensure homogeneity in the data products to the extent possible. All of the PHANGS-HST science-ready drizzled images and coaligned single exposures are available for download at MAST.[38]

---

[35] https://iopscience.iop.org/collections/2041-8205_PHANGS-JWST-First-Results

[36] Parallel imaging with Advanced Camera for Surveys targeting the galaxy halo was also performed to constrain distances by measuring the brightness of the tip of the red giant branch (see Anand et al. 2021; and Section 3.2 of Lee et al. 2022).

[37] LEGUS data products: https://archive.stsci.edu/prepds/legus/dataproducts-public.html.

[38] https://archive.stsci.edu/hlsp/phangs/phangs-hst

Table 1
Exposure Time and Detector Type for Each Band

Galaxy	HST-GO-PID	n_p	F275W	F336W	F435W/F438W		F555W		F814W	
			$t_{\rm exp}$ (s)	$t_{\rm exp}$ (s)	Det	$t_{\rm exp}$ (s)	Det	$t_{\rm exp}$ (s)	Det	$t_{\rm exp}$
IC 1954	15654	1	2083	1059	UVIS	1006	UVIS	649	UVIS	844
IC 5332	15654	1	2089	1061	UVIS	1011	UVIS	650	UVIS	804
NGC 628C	10402, 13364	1	2434	2323	WFC	864	WFC	546	WFC	587
NGC 628E	9796, 13364	1	2311	1102	WFC	2967	UVIS	947	WFC	986
NGC 685	15654	1	1421	712	UVIS	683	UVIS	464	UVIS	554
NGC 1087	15654	1	2095	1067	UVIS	1014	UVIS	649	UVIS	778
NGC 1097	13413, 15654	2	2220	1236	UVIS	805	UVIS	2229	UVIS	697
NGC 1300	10342, 15654	2	2239	2202	WFC	1710	WFC	858	WFC	858
NGC 1317	15654	1	2083	1063	UVIS	1014	UVIS	649	UVIS	805
NGC 1365	15654	1	2101	1071	UVIS	1020	UVIS	646	UVIS	812
NGC 1385	15654	1	2091	1066	UVIS	1015	UVIS	649	UVIS	809
NGC 1433	13364	1	2321	1097	UVIS	950	UVIS	1120	UVIS	970
NGC 1512	13364	3	2315	1095	UVIS	944	UVIS	1119	UVIS	966
NGC 1559	14253, 15145, 15654	1	4330	1062	UVIS	1196	UVIS	1833	UVIS	3514
NGC 1566	13364	1	2329	1102	UVIS	950	UVIS	1127	UVIS	973
NGC 1672	10354, 15654	2	2730	2392	WFC	811	UVIS	1466	WFC	814
NGC 1792	15654	1	2096	1071	UVIS	1018	UVIS	649	UVIS	805
NGC 2775	15654	1	2083	1061	UVIS	1018	UVIS	650	UVIS	792
NGC 2835	15654	1	2095	1064	UVIS	1015	UVIS	648	UVIS	813
NGC 2903	15654	2	2158	1096	UVIS	1039	UVIS	665	UVIS	829
NGC 3351	13364	2	2268	1092	UVIS	1023	UVIS	1421	UVIS	1550
NGC 3621	9492, 15654	2	2237	2210	WFC	687	WFC	687	WFC	917
NGC 3627	13364	2	2200	1092	UVIS	971	UVIS	847	UVIS	861
NGC 4254	12118, 15654	2	2126	1167	UVIS	1023	UVIS	696	UVIS	758
NGC 4298	14913, 15654	1	2136	1867	UVIS	1024	UVIS	2037	UVIS	1026
NGC 4303	15654	1	2097	1070	UVIS	1016	UVIS	651	UVIS	780
NGC 4321	15654	2	2306	1170	UVIS	1108	UVIS	708	UVIS	891
NGC 4535	15654	1	2088	1066	UVIS	1014	UVIS	646	UVIS	789
NGC 4536	11570, 15654	2	2231	1158	UVIS	1080	UVIS	722	UVIS	848
NGC 4548	15654	1	2089	1066	UVIS	1016	UVIS	650	UVIS	804
NGC 4569	15654	1	2088	1064	UVIS	1013	UVIS	648	UVIS	803
NGC 4571	15654	1	2087	1064	UVIS	1015	UVIS	649	UVIS	803
NGC 4654	15654	1	2089	1067	UVIS	1015	UVIS	648	UVIS	803
NGC 4689	15654	1	2077	1062	UVIS	1013	UVIS	647	UVIS	803
NGC 4826	15654	1	2085	1069	UVIS	1015	UVIS	650	UVIS	812
NGC 5068	15654	2	1572	802	UVIS	1023	UVIS	655	UVIS	817
NGC 5248	15654	1	2096	1069	UVIS	1016	UVIS	651	UVIS	792
NGC 6744	13364	2	2250	1099	UVIS	977	UVIS	1099	UVIS	957
NGC 7496	15654	1	2078	1058	UVIS	1008	UVIS	646	UVIS	807

Note. This table presents for each PHANGS-HST galaxy the proposal ID (HST-GO-PID), the exposure time ($t_{\rm exp}$), and number of pointings (n_p) for each band. We also specify the HST instrument/detector used (Det) except for the bands F275W and F336W as they were all observed with the UVIS detector. We abbreviate Advanced Camera for Surveys/WFC as WFC, and WFC3/UVIS as UVIS. For the *B* band, all observations taken with the UVIS (WFC) detector are performed with the filter F438W (F435W).

(This table is available in machine-readable form.)

2.2. Candidate Star Cluster Selection and Photometry

The initial source detection (Thilker et al. 2022) on the HST imaging was performed with a combination of the point-spread function (PSF)-fitting photometry software DOLPHOT[39] (v2.0, Dolphin 2016) and PHOTUTILS/DAOSTARFINDER[40](Bradley 2023), a Python implementation of DAOPHOT[41](v1.3-2 Stetson 1987). A combined "all-source" *V*-band detection catalog was created as described in Thilker et al. (2022). The number of sources detected in each galaxy ranges from 200,000 to 1,200,000, with a median of 300,000.

Star clusters have effective radii between 0.5 and 10 pc (Portegies Zwart et al. 2010; Ryon et al. 2017; Krumholz et al. 2019; Brown & Gnedin 2021). At the distance of our targets, they appear single peaked and are marginally resolved in HST WFC3 images, which have a pixel scale of 0″.04. To distinguish point sources from cluster candidates, multiple concentration indices (Thilker et al. 2022) are computed using *V*-band photometry measured in a series of circular apertures with radii from 1 to 5 pixels. Across all 38 galaxies, a total of ∼190,000 cluster candidates are found. The candidates are inspected and morphologically classified as described in the next section.

---

[39] http://americano.dolphinsim.com/dolphot/

[40] https://photutils.readthedocs.io/en/stable/api/photutils.detection.DAOStarFinder.html

[41] https://www.star.bris.ac.uk/~mbt/daophot/

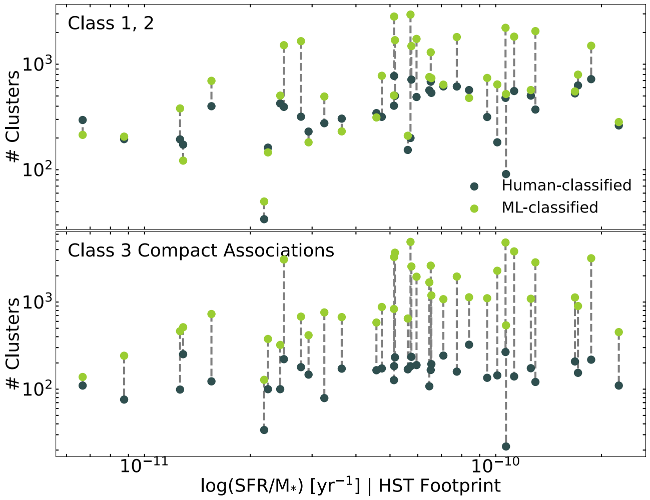

Figure 1. The number of star clusters (top panel) and compact associations (bottom panel) in each of the 38 PHANGS-HST galaxies, shown as a function of the specific star formation rate (sSFR), estimated inside the HST footprint. Sources that have been inspected and classified by a human (co-author B.C.W.) are shown in dark green, while those that have been classified using a neural network model (Hannon et al. 2023) are shown in light green.

Fluxes are computed using photometry in circular apertures with radii of 4 pixels ($\sim 0\farcs16$; which subtends 3.4–18 pc for galaxy distances 5–23 Mpc spanned by the PHANGS-HST sample, see Lee et al. 2022, Table 1). The sky background at the position of each object is estimated in a sky annulus between 7 and 8 pixel radius. To compute total fluxes, we apply a correction for the light outside the aperture, carefully derived for each filter and for each galaxy as described in Deger et al. (2022). The details of the aperture correction can introduce important differences in the colors and derived physical properties of the sources as discussed by Deger et al. (2022).

2.3. Human- and Machine-learning (ML) Morphological Classification

Cluster candidates are inspected to eliminate spurious sources, and to place them into three morphological classes associated with the likelihood of gravitational boundedness for clusters older than the crossing time ∼10 Myr (Whitmore et al. 2010; Gieles & Portegies Zwart 2011; Bastian et al. 2012; Fall & Chandar 2012; Chandar et al. 2014; Grasha et al. 2015; Adamo et al. 2017; Cook et al. 2019; Krumholz et al. 2019; Wei et al. 2020). We use the following commonly adopted classes:

1. class 1 (C1), star cluster—single peak, circularly symmetric, with a radial profile more extended relative to point source;
2. class 2 (C2), star cluster—similar to C1, but elongated or asymmetric;
3. class 3 (C3), compact stellar association—asymmetric, multiple peaks;
4. class 4, not a star cluster or compact stellar association (e.g., image artifacts, background galaxies, individual stars, or pairs of stars).

The reader is referred to Whitmore et al. (2021) for a full description of the PHANGS-HST classification process, and discussion of differences from the LEGUS cluster classification of Adamo et al. (2017). Figures with examples of each of these morphological classes can be found in Wei et al. (2020), Figure 1; Whitmore et al. (2021), Figures 1–4; Lee et al. (2022), Figure 9; Deger et al. (2022) Figures 11–12; and Hannon et al. (2023), Figure 1.

Historically, a bottleneck in the production of extragalactic cluster catalogs has been the visual inspection of candidates. To address this bottleneck, the classification of the ∼190,000 PHANGS-HST cluster candidates was automated using convolutional neural networks (CNNs). CNNs were trained using "deep transfer" ML techniques and samples of human-classified candidates, as discussed in detail in Wei et al. (2020), Whitmore et al. (2021), and Hannon et al. (2023).[42]

To produce the training sets, a human classification was performed for the brightest ∼1000 candidates in each galaxy by co-author B.C.W. As a result, the brightest clusters appear in both the human and ML catalogs, but in galaxies with larger candidate samples, fainter clusters are missing from the human catalog. The ML samples are ∼1 mag (median) deeper in the V band (Whitmore et al. 2021; and Section 3.2), with a range of 16–26 mag. This is an aspect of the human-classified cluster samples that users of the PHANGS-HST catalogs should keep in mind, and leads to a number of key characteristics of the catalogs as discussed in Section 3.

As reported in Hannon et al. (2023), the PHANGS-HST ML and human classifications agreement rates are 74%, 60%, and 71% for C1, C2, and C3, respectively. The model accuracy slightly decreases as the galaxy distance increases ($\lesssim$10% from 10 to 23 Mpc), and as the clusters become fainter (∼10% for $m_v > 23.5$ mag). Whitmore et al. (2021) demonstrated that analyses of mass and age functions are robust to the uncertainties in ML classifications, and also provided essential advice on a science analysis of catalogs based on machine classifications. Differences in the observed properties of the PHANGS-HST catalogs based on human and machine classifications are explored further on later in this paper.

Overall, the performance of our neural network models is comparable to the consistency between human classifiers (Wei et al. 2020; Whitmore et al. 2021), as well as the STARCNET models of Pérez et al. (2021), developed for classification of star clusters in the LEGUS survey (Calzetti et al. 2015; Linden et al. 2022); i.e., 78%, 55%, and 45%. It is important to be aware that there is still significant variation in the classification of C2 and C3 objects among different studies and classifiers (e.g., discussion in Section 6.3.3 of Whitmore et al. 2021). Part of the issue is that the characteristics of the classes have not been documented with detail much beyond the descriptions at the beginning of this section (e.g., see Section 2 in both Adamo et al. 2017; Pérez et al. 2021). To help make progress, in Whitmore et al. (2021), we provide a full description of the methodology and criteria underlying the B.C.W. classification scheme. However, further improvement in classification consistency still requires agreement on the criteria among a full range of experts in the field, and the development of a standardized reference set of human-labeled star clusters, as we discuss in Wei et al. (2020).

---

[42] VISUAL GEOMETRY GROUP (VGG) 19-BN (Simonyan & Zisserman 2015) and RESNET18 (He et al. 2015) network architectures were both explored, although we adopt VGG19-BN for the present work.

2.4. Catalog Structure and Contents

The observed properties of our census of star clusters and compact associations throughout the PHANGS-HST 38 galaxy sample are provided as part of PHANGS-HST Data Release 4/Catalog Release 2 (DR4/CR2) hosted at MAST.[43] Four separate catalogs are provided for each galaxy:

1. human-classified clusters (human C1+C2),
2. ML-classified clusters (ML C1+C2),
3. human-classified compact associations (human C3),
4. ML-classified compact associations (ML C3)

The corresponding physical quantities (ages, masses, reddenings) derived through SED fitting are provided in companion catalogs, as described in Paper II. This catalog structure is motivated by the expectation that the physical quantities may continue to evolve, in particular with the addition of JWST photometry, while the observed properties (from HST) will remain fixed with this release. Thus, overall, 38 (galaxies) × 4 (morphological classification subsets) × 2 (observed or physical properties) catalogs are available.

The C1+C2 clusters are provided separately from the C3 compact associations for two main reasons. First, in studies of star cluster evolution, particularly those that seek to constrain cluster disruption, an analysis is often performed with only C1+C2 single-peaked, centrally concentrated objects, which are thought to have a higher probability of being gravitationally bound, and exclude C3 multipeaked objects (Bastian et al. 2012; Chandar et al. 2014). Terminology was introduced by Krumholz et al. (2019) to facilitate the discussion of the differences in the approaches taken by various groups: C1+C2 samples are referred to as “exclusive” samples, while C1+C2+C3 are referred to as “inclusive samples.” This delineation is explicitly reflected in our catalog structure. Second, the selection methods implemented in the pipeline described above are optimized for the detection of single-peaked clusters, and yield a highly incomplete inventory for multipeaked stellar associations.

Science applications requiring a more complete sampling of the young stellar population should not rely on the C1+C2+C3 catalogs alone. We have developed a second PHANGS-HST pipeline focused on the identification of multiscale stellar associations to address this issue, by deploying a watershed algorithm to segment point-source catalogs into hierarchically nested structures spanning physical scales from 8 to 64 pc (Larson et al. 2023). We find that the majority of C3 objects have a position located within these watershed-identified multiscale stellar associations. Preliminary products from both the PHANGS-HST multiscale stellar association pipeline and the cluster pipeline have been released for five galaxies as part of PHANGS-HST DR3/CR1. The current DR4/CR2 for the full 38 galaxy sample supersedes the preliminary DR3/CR1 cluster catalogs. A complete set of multiscale stellar association data products for the full 38 PHANGS-HST galaxy sample will be published at a later date.

The observed quantities provided in the DR4/CR2 catalogs include the following:

1. persistent IDs to facilitate cross-identification between catalogs, and positional information (object IDs, R.A., decl., image *x, y*),
2. morphological classification (human classification, if available; ML classification for all sources),
3. NUV-*U*-*B*-*V*-*I* aperture photometry (corrected for aperture losses and foreground reddening; provided in Vega magnitudes and mJy; flags for nondetection and lack of HST coverage),
4. standard concentration indices measured in the *V* band.

A listing of these quantities is provided in Table 2, while a full description can be found in the documentation accompanying the DR4/CR2 release at MAST. A discussion of the issues related to the completeness of the catalogs is provided in Section 9.

3. Size and Depth of Cluster Samples

3.1. How Many Star Clusters and Compact Associations Are Found?

A variety of factors determine the number of star clusters and compact associations reported in the PHANGS-HST catalogs. In addition to observational completeness (e.g., due to the depth of the imaging for individual targets, spatial resolution achieved, and selection function imprinted by our catalog production pipeline), the global physical properties of galaxies, in particular the star formation history, influence the properties of the cluster population.

With these factors in mind, and to help visualize the variation in the sizes of the cluster samples across the PHANGS-HST survey, in Figure 1, we show the number of catalog sources as a function of the sSFR ($\mathrm{sSFR} = \mathrm{SFR}/M_*$) evaluated inside the HST footprint.[44] The SFRs are based on an FUV+IR prescription, while the galaxy stellar masses are computed based on an IR flux and mass-to-light ratio (Leroy et al. 2019, 2021).[45] We present clusters of C1 and C2 together in the upper panel and compact associations (C3) in the bottom panel. The human and the ML-classified samples are shown separately, again to illustrate the differences in sample sizes.

The mean size of the human-classified C1+C2+C3 sample per galaxy is ∼560, while for the ML-classified C1+C2+C3 sample it is ∼2500 (∼4 times larger). Human-classified “inclusive” C1+C2+C3 samples span over a factor of 10 in size from 68 in NGC 1317 to 958 in NGC 3627. ML-classified samples of the same variety span an even larger range from 178 in NGC 1317 to 7847 in NGC 3621. This large variation in sample sizes is perhaps the most basic demonstration of the diversity of cluster populations in nearby spiral galaxies.

By construction, the C1+C2 ML-classified sample is significantly larger than the human sample for the majority of galaxies. However, for IC 5332, NGC 685, 2775, 2835, 4571, 4689, and 4826, the human sample contains more C1+C2 clusters than the ML sample. Due to the relatively low number of cluster candidates in these galaxies, all available candidates were classified by co-author B.C.W. The higher number of C1+C2 human classifications are due to differences in the classification determination with the ML algorithm.

For the C3 compact associations, the ML samples are always significantly larger than the human samples (Figure 1 bottom

---

[43] https://archive.stsci.edu/hlsp/phangs/phangs-cat

[44] DSS images with overlays of the HST footprint for each galaxy can be found at https://archive.stsci.edu/hlsp/phangs/phangs-hst.

[45] Also see notes and references provided in Table 1 of Lee et al. (2022).

Table 2
Content Description for the PHANGS-HST DR4/CR2 Observed Property Catalogs of Clusters and Compact Associations

Column Name	Unit	Description
INDEX	int	Running index from 1 to N for each individual target.
ID_PHANGS_CLUSTER	int	PHANGS cluster ID for each individual object classified as class 1,2, or 3, ordered by increasing Y pixel coordinate.
ID_PHANGS_CANDIDATE	int	ID in the PHANGS-HST candidate catalog for each individual target, for cross-identification.
ID_PHANGS_ALLSOURCES	int	ID in the initial PHANGS-HST "all-source" detection catalog for each individual target, for cross-identification.
PHANGS_X	pixel	X coordinates on HST X-pixel grid (0...n-1). Scale = $0\farcs03962$ pixel^{-1}.
PHANGS_Y	pixel	Y coordinates on HST Y-pixel grid (0...n-1). Scale = $0\farcs03962$ pixel^{-1}.
PHANGS_RA	deg	J2000 R.A., ICRS frame, calibrated against selected Gaia sources.
PHANGS_DEC	deg	J2000 decl., ICRS frame, calibrated against selected Gaia sources.
PHANGS_CLUSTER_CLASS_HUMAN	int	Cluster class assigned through visual inspection. Integers 1 and 2 represent C1 and C2 compact clusters. 3 stands for C3 compact associations. Integers >3 are artifacts.
PHANGS_CLUSTER_CLASS_ML_VGG	int	Cluster class determined by VGG neural network. Integers 1 and 2 represent C1 and C2 compact clusters. 3 stands for C3 compact associations. Integers >3 are artifacts.
PHANGS_CLUSTER_CLASS_ML_VGG_QUAL	float	Quality value for "cluster_class_ml" with values between 0.3 and 1, providing the frequency of the mode among the 10 randomly initialized models.
PHANGS_[BAND]_VEGA	mag	HST-band apparent vega magnitude, Milky Way (MW) foreground reddening and aperture corrected. Set to −9999 if source is not covered by HST filter.
PHANGS_[BAND]_VEGA_ERR	mag	Uncertainty of "[BAND]_VEGA."
PHANGS_[BAND]_mJy	mJy	HST-band flux in mJy, MW foreground reddening and aperture corrected. Set to −9999 if source is not covered by HST filter.
PHANGS_[BAND]_mJy_ERR	mJy	Uncertainty of "[BAND]_mJy."
PHANGS_NON_DETECTION_FLAG	int	Integer denoting the number of bands in which the photometry for the object was below the requested signal-to-noise ratio (S/N = 1). 0 indicates all five bands had detections. A value of 1 and 2 means the object was detected in four and three bands, respectively. By design, this flag cannot be higher than 2.
PHANGS_NO_COVERAGE_FLAG	int	Integer denoting the number of bands with no coverage for object. The specific bands that can be identified as photometry columns are set to −9999.
PHANGS_CI	float	Concentration index: difference in magnitudes measured in 1 and 3 pix radii apertures.
CC_CLASS	str	Flag to identify in which region on the color–color diagram the object was associated with. Values are "YCL" (young cluster locus), "MAP" (middle-aged plume), "OGCC" (old globular cluster clump), or "outside" (outside the main regions and therefore not classified). A detailed description is found in Section 4.4.

Note. Source positions were determined in the V band at the detection stage, generally stemming from the DOLPHOT PSF-fitting photometry measurements and have not been optimized with post facto centroiding or fitting of extended source models. This can cause source positions to be shifted slightly (∼1 pixel) from the true location, but has negligible influence on our photometry due to use of a 4 pixel radius aperture. Upcoming structural fitting of C1+C2 clusters, for the purpose of measuring effective radii, will refine source positions. ICRS is the International Celestial Reference System.

panel). These large numbers are likely due to a combination of two factors. First, we deploy our neural network models to classify the full candidate list, and the ML samples thus reach a fainter magnitude limit. (Recall that our ML samples are a median of ∼1 mag deeper in the V band as discussed in Section 2.3; we examine this further in the next section.) Since the mass function of clusters and associations rises as $dN/dM \propto M^{\beta}$, where $\beta \sim -2$ (Krumholz et al. 2019, and references therein), there will be a factor of 100 increase in the number of sources for every additional decade of mass probed (or, up to a factor of 40 increase for every additional magnitude probed). Second, the C3 compact associations in our catalogs tend to be young ($\lesssim$10 Myr, e.g., Lee et al. 2022; see also Section 4.4). For a fixed magnitude limit, these young populations can be detected to much lower masses (between ∼0.5 and ∼2.5 dex lower, depending on the age of the comparison population) due to the high light-to-mass ratios of massive O and B stars, as illustrated in mass–age diagrams for star clusters (e.g., Cook et al. 2019, Figure 13).

In general, the number of clusters and associations found in each galaxy increases with the sSFR. A further analysis of the variation in cluster populations with SFR is provided in Section 5.

3.2. *V-band Magnitude Distributions*

Table 3 shows the median, minimum, and maximum absolute V-band magnitude (M_V) for the human and ML samples. In the absence of a completeness analysis based on (computationally expensive) recovery simulations with artificial star clusters (e.g., Mayya et al. 2008; Adamo et al. 2017; Messa et al. 2018; Linden et al. 2021, 2022; Tang et al. 2023), these statistics provide an

Table 3

Number Count and Absolute Magnitude (M_V) Catalog Statistics

Galaxy	Candidates		Human Classified				ML Classified				M_V^{Hum}	M_V^{ML}
	N_{Cand}	N_{Insp}	C1	C2	C3	C1 + 2 + 3	C1	C2	C3	C1 + 2 + 3	min[mid]max (mag)	min[med]max (mag)
IC 1954	1536	560	37	117	169	323	47	163	647	857	−11.6|−7.3|−6.5	−11.6|−6.9|−5.7
IC 5332	1432	628	78	152	147	377	35	147	416	598	−9.4|−6.0|−5.3	−9.4|−5.9|−5.1
NGC 628C	7725	1308	263	225	188	676	534	1201	1953	3688	−10.7|−7.6|−7.0	−10.7|−6.2|−5.3
NGC 628E	2321	283	51	40	22	113	165	357	540	1062	−10.3|−7.5|−7.0	−10.3|−5.8|−4.9
NGC 685	1568	704	111	194	172	477	63	168	672	903	−12.2|−7.9|−7.1	−12.2|−7.8|−6.9
NGC 1087	2636	976	278	226	174	678	185	384	1091	1660	−11.9|−7.8|−7.0	−11.9|−7.5|−6.3
NGC 1097	7139	1182	417	198	159	774	1037	772	1962	3771	−13.1|−8.1|−7.2	−13.1|−6.4|−4.7
NGC 1300	3602	892	169	149	179	497	830	824	680	2334	−11.2|−8.0|−7.4	−11.2|−6.8|−5.7
NGC 1317	401	180	16	18	34	68	18	32	128	178	−11.3|−8.1|−6.9	−11.3|−8.3|−6.7
NGC 1365	3291	1510	362	267	154	783	353	443	900	1696	−15.1|−8.7|−7.5	−15.1|−7.9|−6.8
NGC 1385	2531	958	269	260	208	737	204	348	1129	1681	−13.1|−8.1|−7.2	−13.1|−7.8|−6.5
NGC 1433	2083	646	90	104	99	293	148	233	463	844	−11.5|−7.9|−7.3	−11.5|−6.9|−6.1
NGC 1512	2675	925	188	120	116	424	220	349	648	1217	−12.8|−7.9|−7.0	−12.8|−6.8|−5.4
NGC 1559	8603	1592	419	303	218	940	657	839	3181	4677	−13.9|−8.9|−7.9	−12.9|−7.7|−6.1
NGC 1566	9045	1752	393	291	166	850	706	591	2619	3916	−13.8|−8.4|−6.5	−13.8|−7.4|−6.0
NGC 1672	8754	1419	238	134	121	493	930	1127	2855	4912	−13.9|−9.3|−8.4	−13.9|−7.1|−5.7
NGC 1792	4641	1215	265	301	108	674	255	501	1683	2439	−12.3|−8.7|−7.1	−12.3|−8.0|−6.6
NGC 2775	628	628	136	160	110	406	106	108	138	352	−11.4|−8.2|−7.2	−11.4|−8.2|−7.2
NGC 2835	3582	1567	223	346	324	893	110	369	1134	1613	−10.7|−7.1|−6.4	−10.7|−7.0|−6.1
NGC 2903	10,837	1156	248	253	232	733	564	1126	3687	5377	−13.3|−8.1|−7.4	−13.3|−6.5|−5.1
NGC 3351	4766	1562	140	177	173	490	238	539	878	1655	−13.3|−7.0|−5.9	−13.3|−5.7|−4.6
NGC 3621	20,347	1307	71	129	183	383	1148	1804	4895	7847	−12.2|−7.8|−7.2	−12.2|−5.4|−3.9
NGC 3627	10,673	1522	462	312	184	958	1134	1694	3287	6115	−12.9|−8.4|−7.8	−12.9|−7.0|−5.4
NGC 4254	12,284	1273	255	225	267	747	659	1554	4824	7037	−12.8|−8.7|−8.1	−12.8|−7.2|−5.5
NGC 4298	2272	547	173	103	79	355	161	333	760	1254	−11.4|−7.5|−6.9	−11.4|−6.6|−5.2
NGC 4303	9967	1192	264	293	140	697	439	1385	3813	5637	−12.6|−9.4|−8.7	−12.6|−7.9|−6.6
NGC 4321	6725	1381	436	279	235	950	521	965	2563	4049	−14.2|−8.2|−7.4	−12.6|−7.2|−5.9
NGC 4535	2648	972	202	202	127	531	196	310	833	1339	−12.4|−7.8|−7.0	−12.4|−7.4|−6.5
NGC 4536	3120	750	127	189	135	451	216	525	1106	1847	−12.0|−7.7|−7.1	−12.0|−6.9|−5.7
NGC 4548	788	414	96	99	76	271	100	106	242	448	−10.7|−7.5|−6.6	−10.7|−7.4|−6.4
NGC 4569	1309	726	212	213	100	525	228	276	322	826	−11.2|−7.7|−7.0	−11.2|−7.6|−6.7
NGC 4571	1085	465	61	101	100	262	44	102	377	523	−10.0|−7.2|−6.4	−9.9|−7.1|−6.2
NGC 4654	2812	1272	256	360	243	859	182	458	1079	1719	−13.4|−8.6|−7.7	−13.4|−8.3|−7.3
NGC 4689	1580	783	130	214	165	509	99	214	582	895	−11.0|−7.3|−6.4	−11.0|−7.2|−6.2
NGC 4826	1935	928	62	111	252	425	48	74	514	636	−10.0|−5.7|−4.3	−9.6|−5.6|−4.3
NGC 5068	6319	957	54	128	144	326	69	574	2286	2929	−10.0|−6.8|−6.1	−9.5|−5.0|−3.9
NGC 5248	3434	1154	211	324	194	729	232	506	1192	1930	−13.2|−7.7|−6.9	−12.0|−7.3|−6.2
NGC 6744	10,276	1436	221	173	221	615	393	1122	3079	4594	−10.3|−6.9|−6.4	−10.3|−5.7|−4.4
NGC 7496	1390	618	105	158	110	373	72	211	452	735	−13.6|−7.7|−6.9	−12.3|−7.5|−6.4
Median	3120	972	202	194	165	509	216	443	1079	1681	−12.2|−8.1|−7.0	−12.0|−7.0|-6.0
Mean	4840	1008	199	196	159	555	342	585	1528	2456	…	…
Total	188,760	39,340	7789	7648	6228	21,665	13,346	22,834	59,610	95,790	…	…

Note. This table presents the number of star cluster candidates N_{Cand}, the number of human inspected candidates N_{Insp}, and the number of class 1, 2, and 3 objects (C1, C2, C3) resulting from the human and ML morphological classifications in the catalogs for each of the 38 PHANGS-HST galaxies (39 fields—the sources in NGC 628 are reported in two separate catalogs). The minimum, median, and maximum absolute V-band total magnitude (corrected for foreground MW reddening and aperture losses) are also given for the total C1+C2+C3 human and ML samples. The last three rows provide the median, mean, and total numbers of objects summed over all 38 galaxies.

(This table is available in machine-readable form.)

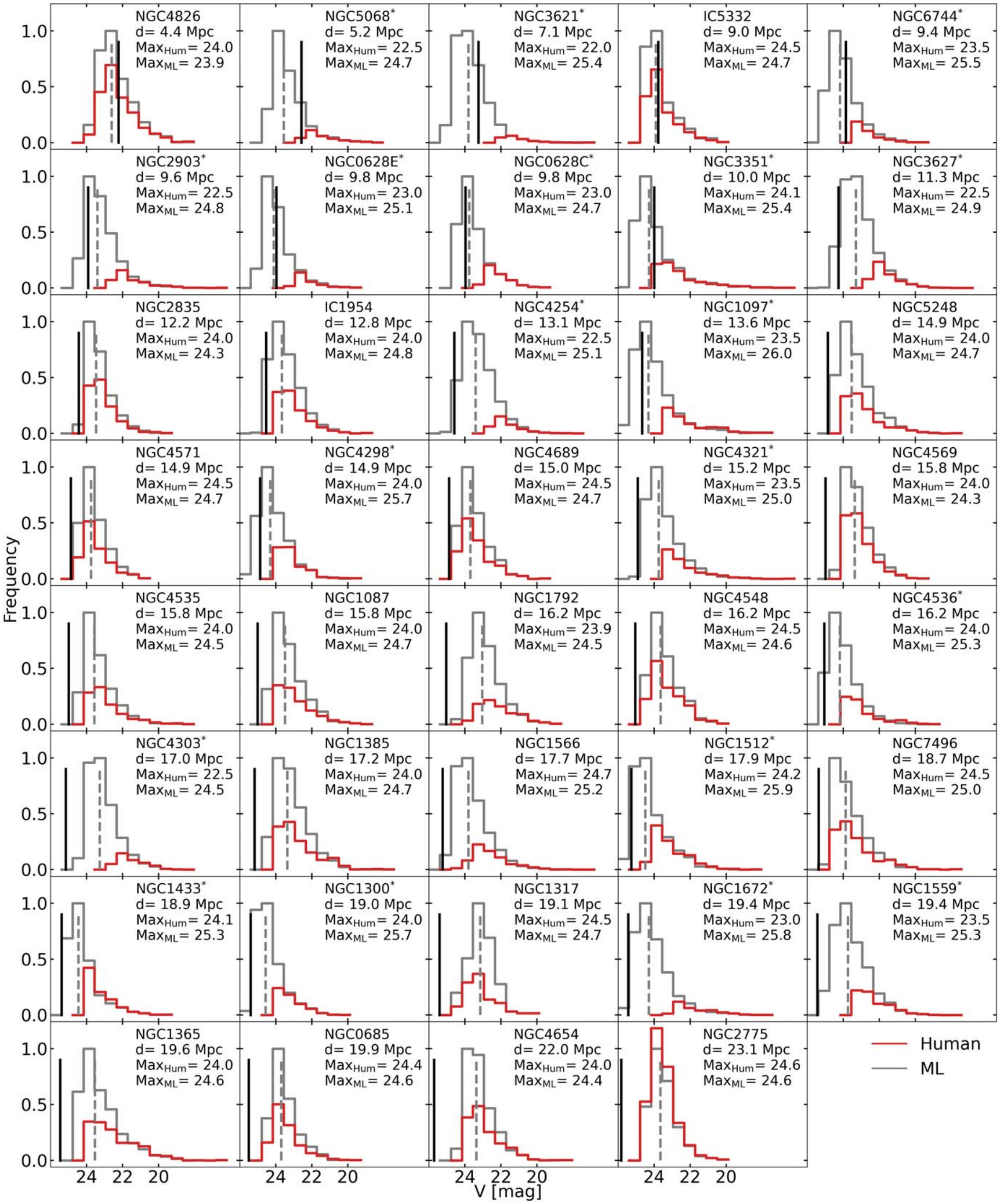

Figure 2. Probability distributions of apparent total *V*-band magnitude (i.e., corrected for aperture losses) for the cluster (class $1+2$) and compact association (class 3) populations in all 38 PHANGS-HST galaxies. We show with red (gray) the human- (ML) classified catalogs. In order to compare their distribution, we normalized the histograms to the highest bin of the ML sample. For each target, we display the distance and the faintest detected magnitude for the human and the ML-classified clusters. A gray dashed line shows the median ML *V*-band magnitude, and the solid black line the limit of $M_v = -6$ used as the lower magnitude cut in Adamo et al. (2017). We mark targets with a star, if the faintest human detected magnitude is brighter than the median ML detected magnitude.

estimate of the depth of the cluster samples for each galaxy. In Figure 2, we show histograms of the apparent *V*-band magnitude (m_V) for the clusters and associations in each of the galaxies in the PHANGS-HST sample. The panels are ordered by increasing galaxy distance, and the human and the ML samples are shown separately.

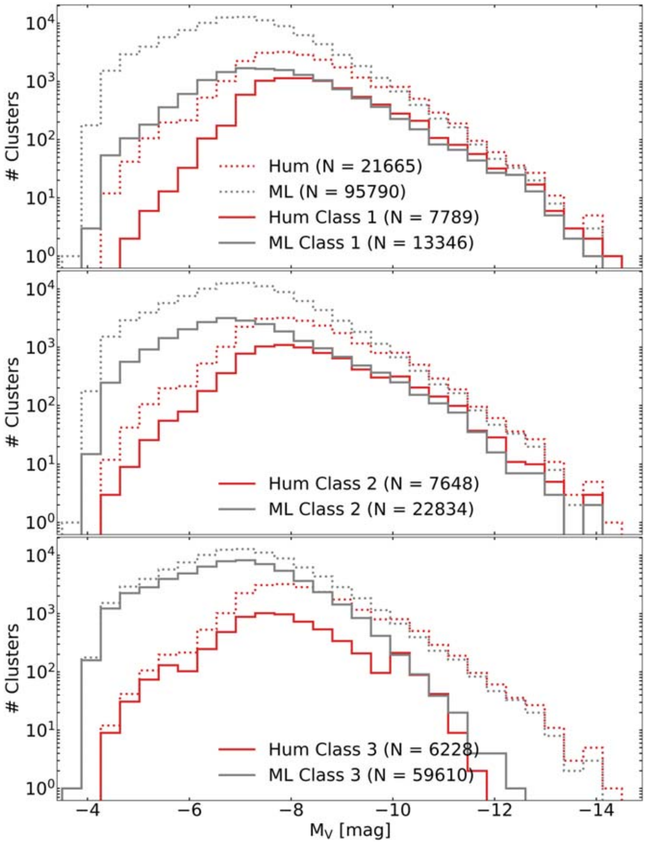

Figure 3. Distribution of the absolute *V*-band magnitude of the human (red) and the ML (gray) samples for class 1 + 2 + compact associations shown as dotted lines in all three panels. To visualize individual cluster classes, we show their distributions with solid lines in each panel. The histograms are shown in logarithmic scale to visualize the zone where both samples have comparable sizes, as well as the differences when the machine-learning sample size increases toward fainter magnitudes.

In 18 out of 38 galaxies, the human-classified sample is shallower (by ∼2 mag) than the ML sample, which is a direct result of our strategy of only providing human classifications for the brightest clusters. For these galaxies (marked with a star next to their names in Figure 2), the faintest object in the human-classified sample is brighter than the median magnitude of the ML-classified sample.

Figure 3 shows histograms of the absolute *V*-band magnitude M_V for all C1 clusters, C2 clusters, and C3 compact associations aggregated across the 38 galaxies, with the human and the ML samples shown separately. We also show the M_V distribution for each class individually. The distributions for the human and the ML samples are consistent for the brightest objects up to an absolute magnitude of $M_V \sim -10$. After that, the distributions diverge. We note that there is a larger difference between human- and ML-classified objects at fainter magnitudes for C2 clusters and even more for C3 compact associations in comparison to C1 clusters. This is due to the fact that the ML sample is deeper than the human sample, and C1 clusters are on average older than C2 clusters, with C3 compact associations representing the youngest objects (see Section 4.1). As just discussed in Section 3.1, a larger number of C2 clusters and C3 compact associations will be detected at fainter magnitudes due to a combination of lower mass-to-light ratio at young ages and the shape of the cluster mass function. For the aggregate human and the ML samples, the median absolute *V*-band magnitude is −8.1 and −7.0 , and their 99th percentiles are −5.5 and −4.5, respectively. Thus, when combined across the 38 galaxies, the ML sample is about 1 mag deeper in the *V* band than in the human sample.

We note that, at the bright end, the aggregate ML sample has 406 fewer C1+C2+C3 objects than the human sample for $M_V < -10$ mag, and this is generally consistent with the accuracy of the ML classifier (Hannon et al. 2023). In cases where a human classification exists, it is preferred for most science applications relative to the ML classification.

The detection limit depends primarily on the distance of the target since the exposure times for all new HST observations (i.e., as opposed to recycled archival data) were generally uniform (Table 1). In Figure 4, we plot the brightest, median, and faintest absolute *V*-band magnitude, and corresponding quantities for the stellar masses for the C1+C2 samples, in each galaxy as a function of the galaxy distance. The stellar mass is estimated through SED fitting of the five filter UV–optical PHANGS-HST photometry as described in Thilker et al. (2024). In the upper left panel of Figure 4, the galaxies where the human-classified sample is far shallower are indicated with open circles, consistent with the annotation provided in the Figure 2 histograms. In Figure 5, we present a montage showing the brightest cluster in each of our targets. These luminous clusters are almost all very young (1–3 Myr), although a few middle-age objects and one globular cluster (in NGC 2775) are also in the sample.

Our catalogs will of course include a population of fainter star clusters in the galaxies, which are closer to us, and which are not detectable in the more distant targets. The median absolute *V*-band magnitude is −6.6 mag for C1+C2 ML clusters below a distance of 14 Mpc. At distances >14 Mpc, the median absolute *V*-band magnitude is −7.7 mag. The medians for the human-classified samples are −7.9 mag for galaxies at distance <14 Mpc, and −8.4 mag for those that are farther away. In terms of stellar mass, we find median stellar masses of $\log(M_*/M_\odot) = 3.9$ and 4.3 for ML and human clusters, respectively, at distances <14 Mpc. For the more distant clusters (>14 Mpc) we find median $\log(M_*/M_\odot) = 4.3$ and 4.6.

4. Color–Color Diagrams: The PHANGS-HST 38 Galaxy Aggregate Distribution

The SED of a single-age stellar population (or simple stellar population, hereafter SSP) evolves over time such that young populations (∼10 Myr) are dominated by blue light from massive stars (e.g., brighter in the NUV or *U* band), while old stellar populations (∼1 Gyr) are dominated by red light from lower mass MS and evolved intermediate mass stellar populations (e.g., brighter in the *I* band). Hence, the distributions of star clusters in color–color diagrams have long been studied to gain insight into the properties and evolution of the cluster population (e.g., van den Bergh & Hagen 1968; Searle et al. 1980; Girardi et al. 1995; Larsen & Richtler 1999; Chandar et al. 2010; Adamo et al. 2017), as well as to test SSP models (e.g., Maraston 1998; Bruzual & Charlot 2003; Vázquez & Leitherer 2005).

Our large sample of ∼100,000 star clusters and associations combined across the 38 galaxies of the PHANGS-HST sample reveals that the distribution in the $U-B$ versus $V-I$ color–color diagram can be described in terms of three main features: a young cluster locus (YCL), a middle-age plume (MAP), and

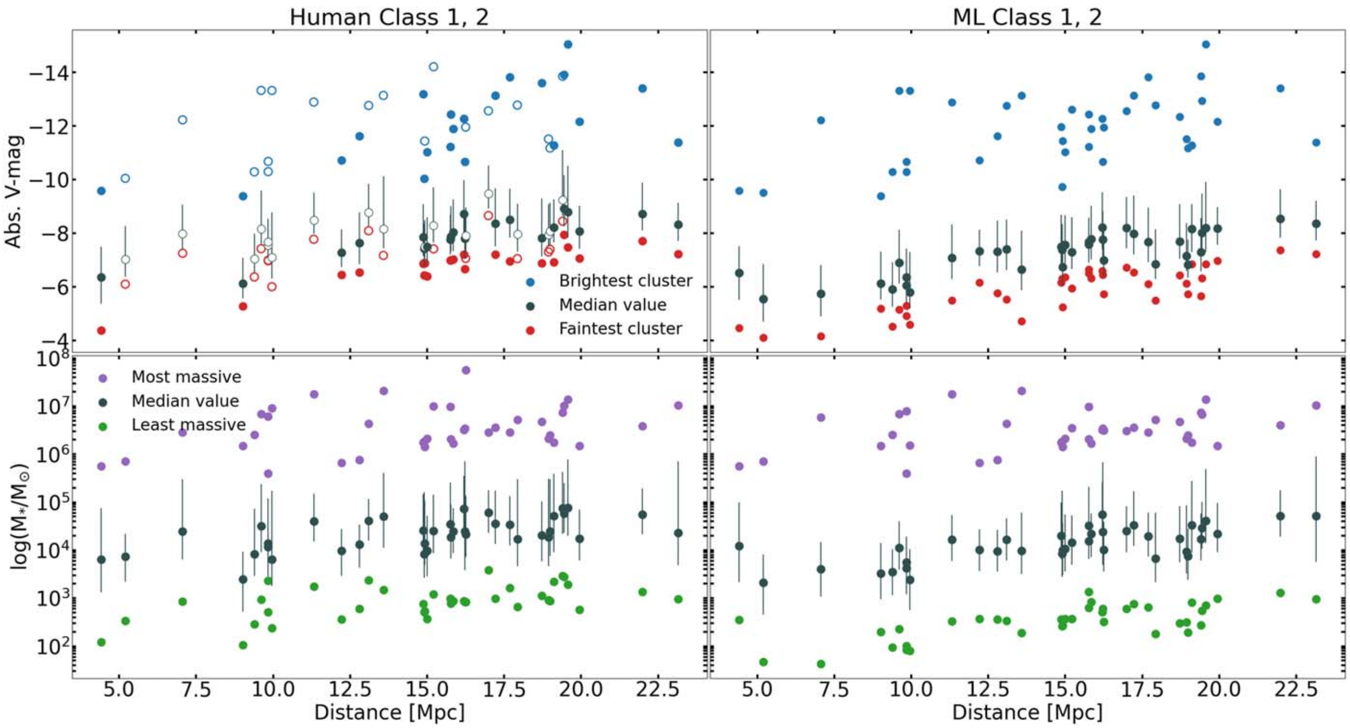

Figure 4. Absolute *V*-band magnitude (top panels) and stellar mass (bottom panels) as function of galaxy distance. The left (respectively right) panels are for human- (respectively ML) classified star clusters (class 1 + 2) for each galaxy. Gray dots with error bars denote the median value and the 16–84 percentile range, red (respectively blue) dots represent the brightest (respectively faintest) *V*-band magnitude. The most (respectively least) massive clusters are shown with violet (respectively green) dots. In the top left panel, we use open circles, if the maximal human detected magnitude is brighter than the median ML detected magnitude (see Figure 2).

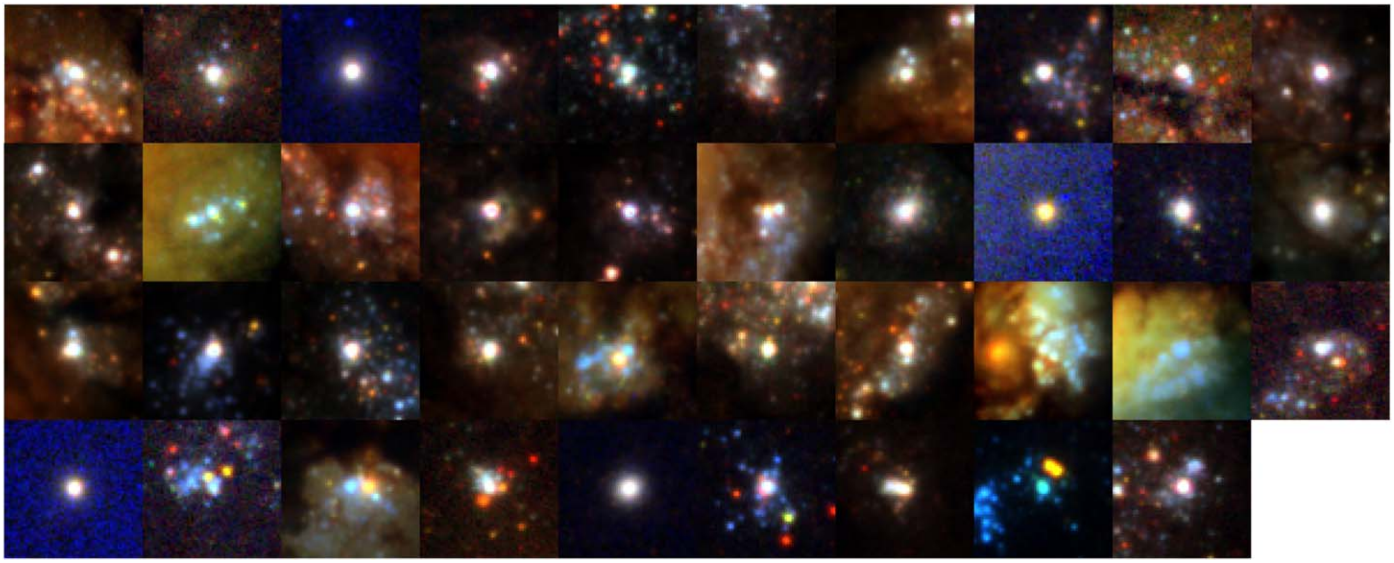

Figure 5. The brightest (absolute *V*-band magnitude, uncorrected for internal extinction) cluster in each PHANGS-HST target. Color images are constructed from *I*-, *V*-, and *U*-band data, and each cutout spans 2.″38 (corresponding to ∼50–270 pc, depending on the distance to each galaxy). The clusters are arranged from left to right, top to bottom in the order of Table 3.

an old globular cluster clump (OGC). Here, we examine variations in these features for

1. different color combinations (NUV-*B*-*V*-*I* and *B*-*V*-*I* as well as standard *U*-*B*-*V*-*I*),
2. the three morphological classes of clusters and compact associations,
3. the ML- and human-classified samples,
4. low- and high-mass samples,
5. the individual 38 galaxies in the survey.

4.1. Comparison of the C1, C2, C3 Morphological Classes and Different Color Combinations

We begin by presenting color–color diagrams formed from NUV-*B*-*V*-*I*, *U*-*B*-*V*-*I*, and *B*-*V*-*I* photometry for clusters

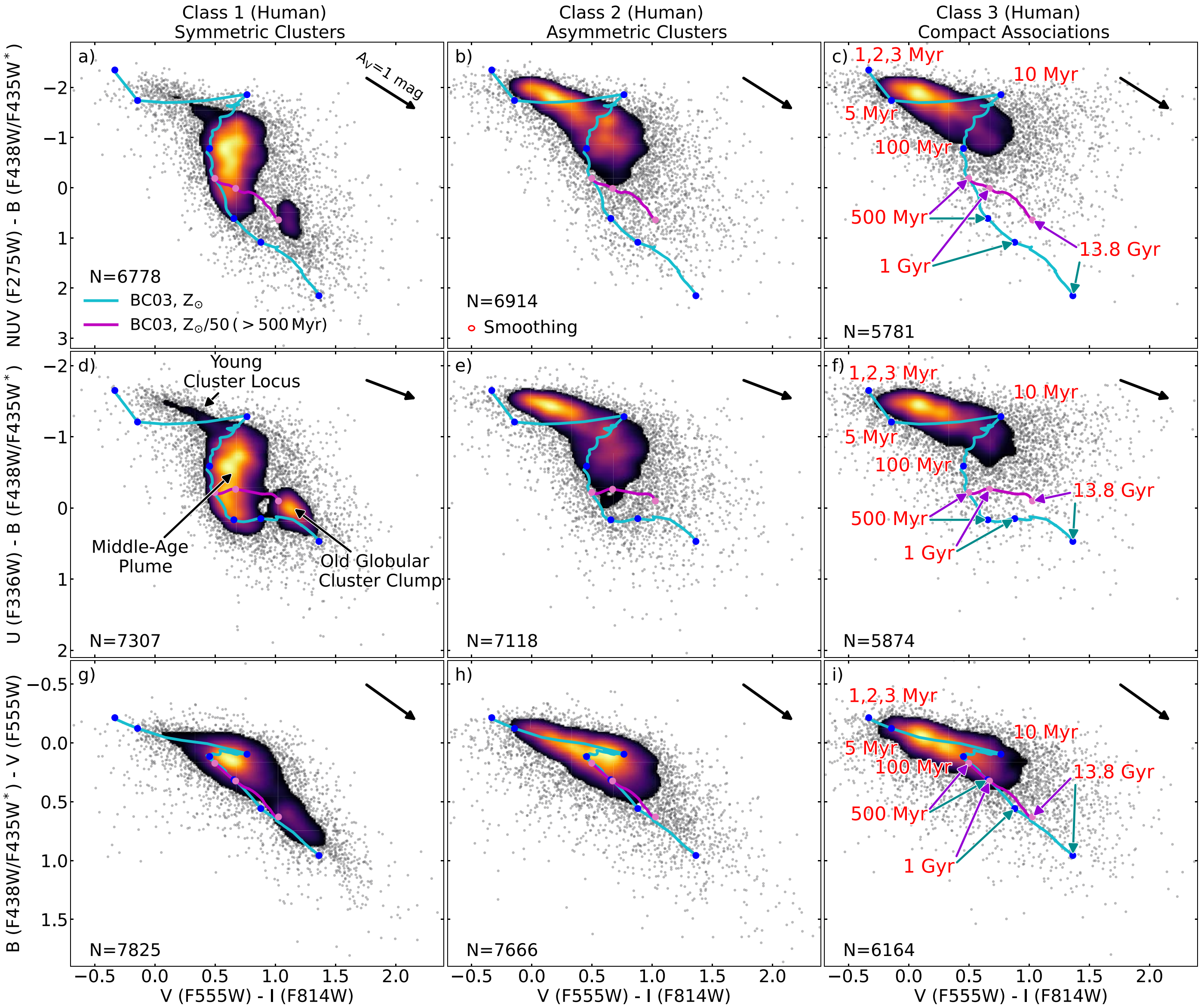

Figure 6. Color–color diagrams for the PHANGS-HST human-classified sample, with each morphological class shown separately: C1 single-peaked symmetric clusters (left column); C2 single-peaked asymmetric clusters (middle column); and C3 multipeaked compact associations (right column). In all panels, $V-I$ is plotted along the horizontal axis, and three other colors are shown along the vertical axis: NUV-B (top row), $U-B$ (middle row), and $B-V$ (bottom row). We only show data points for clusters that are detected with at least an S/N > 3 in the plotted bands. Individual clusters are represented by black dots whereas in crowded regions we show a Gaussian-smoothed heat map indicating the relative density. The size of the smoothing kernel is shown by a red circle on the top middle panel. A cyan track denotes the BC03 SSP model for $Z_\odot$ metallicity at ages from 1 Myr until 13.7 Gyr. The portion of the SSP track $Z_\odot/50$ metallicity from 0.5 to 13.7 Gyr is also shown with a magenta track. Key ages are indicated on the right column and are marked with blue and pink dots on each track. A reddening vector (top right of each panel) corresponds to $A_v = 1.0$ mag. In panel (d), we indicate names for relevant loci in the color–color space.

and compact associations in the three human-determined morphological classes (Figure 6). As in our previous papers (e.g., Turner et al. 2021; Deger et al. 2022; Lee et al. 2022), we examine the color–color diagram in the context of BC03 SSP model tracks with no addition of nebular emission, and the dust reddening vector. We show SSP models of $Z_\odot$ and $Z_\odot/50$ metallicity since it has been well established by past studies including PHANGS-MUSE that the spiral galaxies, both in our sample and more generally, have nebular metallicities around $Z_\odot$ (e.g., Zaritsky et al. 1994; Skillman et al. 1996; Moustakas et al. 2010; Groves et al. 2023; Scheuermann et al. 2023), and because our catalogs include objects with a full range of ages, including old globular clusters, which are metal poor. The $Z_\odot/50$ metallicity BC03 models (based on the Padova 1994 tracks) correspond to [Fe/H] = 1.65, which should generally cover the range of globular cluster metallicities for spiral galaxies (Brodie & Strader 2006, and references therein).

An examination of Figure 6, where the human-classified C1, C2, and C3 samples are shown in separate panels, provides insight into how the three morphological classes map onto cluster physical properties.

The C1 single-peaked symmetric clusters are predominantly older than ~10 Myr (Figure 6 left panels). Both the MAP and OGC are evident in the NUV-B versus $V-I$, and $U-B$ versus $V-I$ diagrams of the C1 population (Figures 6(a) and (d)). Although there are younger C1 clusters that define a sharp diagonal locus roughly parallel to the reddening vector in the

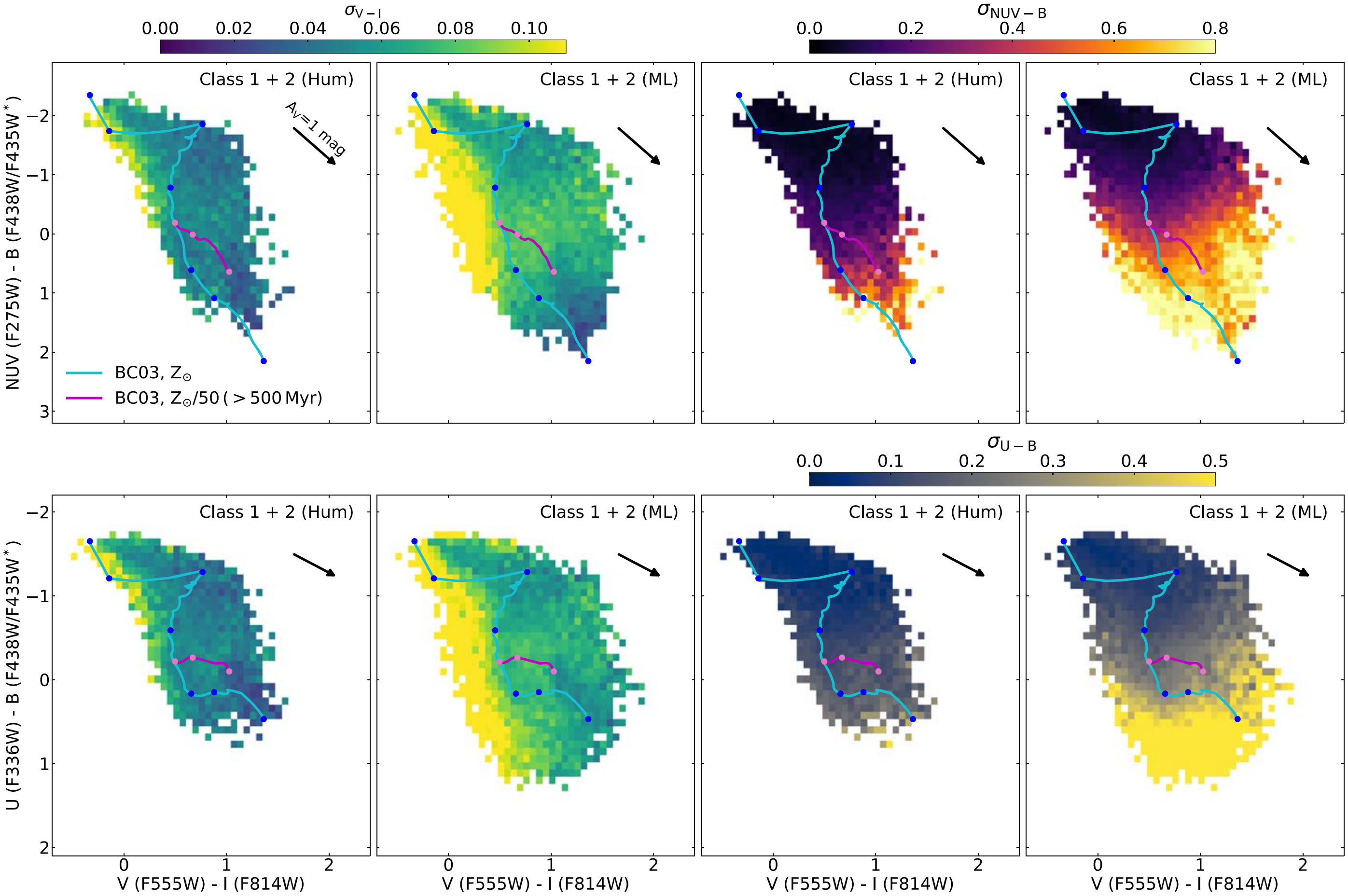

Figure 7. Mean color uncertainties for the NUV-B vs. $V-I$ (top row) and $U-B$ vs. $V-I$ (bottom row) diagrams. We present class 1 + 2 clusters for ML (left two panels) and human classifications (right two panels) separately. The maps show the mean uncertainty in each bin, and only bins with at least five clusters are displayed.

$U-V$ versus $B-I$ diagram (Figure 6(d)), these objects are in the minority of the C1 population.

In contrast, the populations of C2 single-peaked asymmetric clusters and C3 multipeaked compact associations are predominantly young, and both show a prominent, clearly defined YCL, which again appears to be roughly parallel to the reddening vector. The C2 sample YCL exhibits an extension into the MAP to ∼500 Myr (Figures 6(b) and (e)). The shape of the left side of the extension, which follows the BC03 SSP track, suggests that this distribution contains middle-age clusters, which are not solely reddened young clusters. The C3 YCL human-classified (bright) sample does not have an obvious extension into the MAP.

In the $B-V$ versus $V-I$ diagrams, the three main features are blended and far less distinct (Figure 6 bottom row); this reaffirms the need for NUV and U-band photometry for cluster age dating (Smith et al. 2007). After 100 Myr, not only is the reddening vector parallel to the $B-V$ versus $V-I$ SSP track, but the solar and subsolar metallicity SSP models trace a similar path (Figure 6(i)). The NUV band (F275W) is the shortest wavelength filter available on the HST WFC3 camera that avoids the 2175 Å dust feature, while the U and B bands straddle the 4000 Å break. The combination of the NUV-U-B-V-I filters serves to break the age–extinction–metallicity degeneracy, as illustrated by the untangling of the SSP tracks in the NUV-B versus $V-I$ (top row) and $U-B$ versus $V-I$ (middle row) planes, and by the separation of metal-rich and metal-poor tracks, as reflected in the segregation of the OGC from the MAP.

Hereafter, we choose to focus on the $U-B$ versus $V-I$ color–color diagram. While the separation between the MAP and the OGC is larger in the NUV-B versus $V-I$ plane, the NUV detection rate and signal-to-noise ratio (S/N) for old clusters (which are significantly dimmer in the blue) are lower relative to the U band (Figure 7) despite the factor of ∼2 larger NUV exposure time (Table 1).

4.2. Comparison of Human- and Machine-learning-classified Samples

As discussed earlier, by construction, an important difference between the human- and ML-classified catalogs is the depth of the samples. Whitmore et al. (2021) looked for other possible systematic differences between the ML- and human-classified samples, and assessed the performance of the ML classifications by examining the UVBI color–color diagram of five individual galaxies processed with the first generation of our CNN models (Wei et al. 2020).[46] Here, we compare the samples aggregated over all 38 galaxies, and classified using the current version of our CNN model (Hannon et al. 2023).[47]

---

[46] DR3/CR1 at https://archive.stsci.edu/hlsp/phangs/phangs-cat.

[47] DR3/CR2 at https://archive.stsci.edu/hlsp/phangs/phangs-cat.

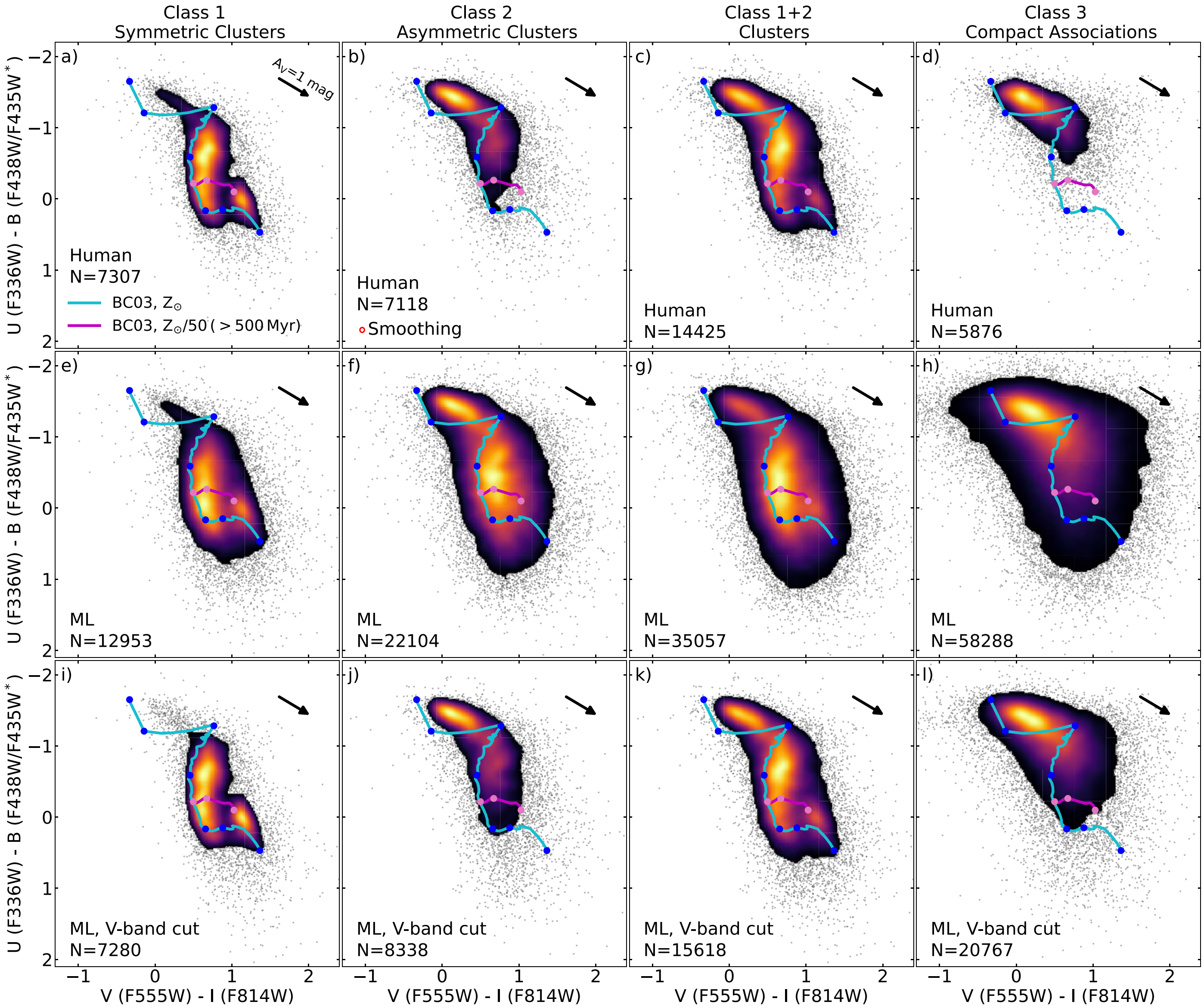

Figure 8. Color–color diagrams for the human cluster sample (top row) and the ML cluster sample (middle and bottom rows). In the middle row, we show all ML-classified clusters, whereas the bottom row only shows ML-classified clusters up to the same *V*-band magnitude for each target as detected for the human sample. The individual *V*-band cuts are estimated with the maximal detected magnitude as presented in Figure 2. Cluster classes 1, 2, 1 + 2, and 3 compact associations are shown individually in each column from left to right, respectively. Clusters are represented by black dots and in crowded regions by a Gaussian-smoothed heat map indicating the relative density.

In Figure 8, we compare the $U - B$ versus $V - I$ diagram for each cluster class for the human (top row) and the ML samples (middle and bottom rows). In the bottom row, a *V*-band magnitude cut corresponding to the depth of the human-classified sample (as indicated in Figure 2) is applied to the ML sample for each individual galaxy. Qualitatively, it appears that this magnitude cut results in the same color–color features seen in the human-classified sample, which provides evidence for the robustness of the ML classifications for the brighter sources.

For the C1 clusters, the OGC shows a slightly broader distribution for the full ML sample (compare Figures 8(a) and (e)). This slightly broader distribution is mostly due to the fact that fainter globular clusters in the ML sample are detected in the U and B bands, but have low S/N. These fainter clusters in the ML samples also appear to shift the peak of the MAP toward older ages (compare Figures 8(a) and (e)). For the C2 clusters, the increase of fainter sources in the ML sample results in a prominent MAP, which were underrepresented in the human-classified sample, but does not result in a distinct OGC (compare Figures 8(b) and (f)).

A comparison of the human- and ML-classified C3 compact associations shows a significantly broader distribution for the ML sample stretching over the entire color–color diagram (compare Figures 8(d) and (h)). The broadening of the distribution is not surprising given that the ML C3 sample (1) is dominated by young populations and will probe to lower masses relative to the C1/C2 samples (as discussed in Section 3.1), and (2) will thus have the lowest mean S/N values. We find about 4 times as many ML C3s when applying the human-classified catalog *V*-band magnitude limit. For the human-classified sample, C3s are the smallest category ($N = 6235$, 28%); however, for the ML-classified sample, it is by far as the largest category ($N = 59{,}684$, 62%). The low-

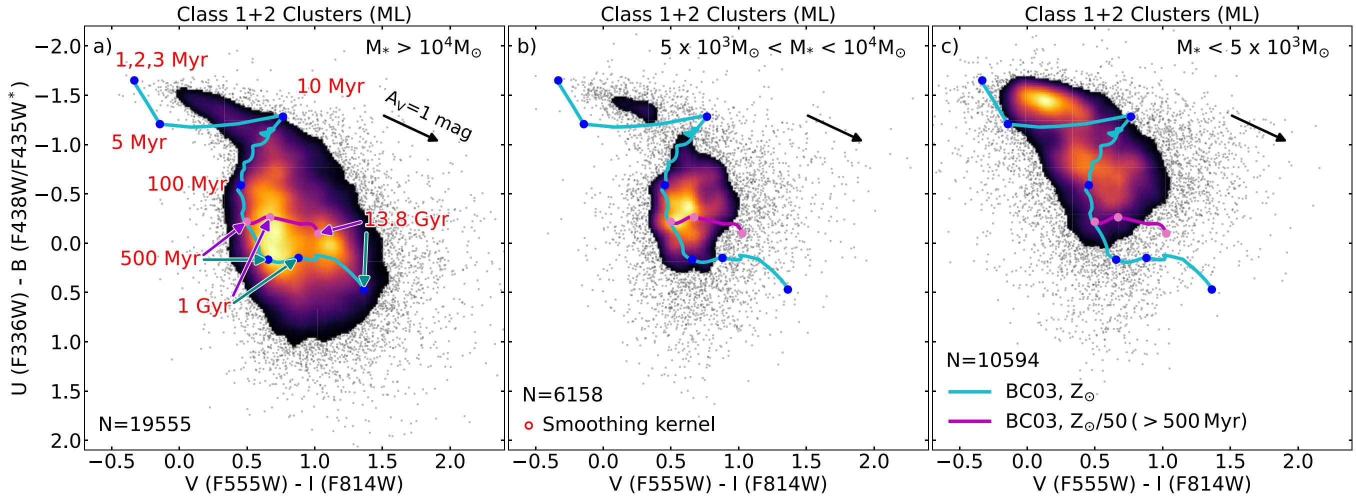

Figure 9. Color–color diagram of ML-classified class 1 and 2 clusters in three bins of stellar mass. The most massive clusters with $M_* > 10^4\, M_\odot$ are shown in the left panel, intermediate masses of $5 \times 10^3 M_\odot > M_* < 10^4 M_\odot$ are in the middle panel, and low-mass clusters of $M_* < 5 \times 10^3 M_\odot$ are in the right panel. Similar to Figure 6, we use a density heat map to illustrate the distribution of clusters.

mass ML C3 associations ($<10^4 M_\odot$) will also be affected by stochasticity in sampling of the stellar initial mass function (IMF; e.g., Fouesneau & Lançon 2010; Popescu et al. 2012; de Meulenaer et al. 2013; Krumholz et al. 2015; Orozco-Duarte et al. 2022), which leads to large scatter in their luminosities and colors relative to the predictions of the BC03 SSP model track, which assumes a fully sampled IMF.

4.3. Comparison of High- and Low-mass Clusters

To further explore the impact of stellar IMF stochasticity on the observed properties of low-mass clusters, in Figure 9, we present the color–color diagram for the C1+C2 aggregate sample in three different mass bins.

The differences in the predominance of the YCL, MAP, and OGC in the three mass bins are primarily due to the dependence of the mass limit with age. As discussed at the end of Section 3.1, for a fixed magnitude limit, due to evolution of the mass-to-light ratio, the YCL ($<10^7$ Myr) can be detected to masses 100 times lower than the OGC (>1 Gyr), as illustrated in mass–age diagrams for star clusters (e.g., Cook et al. 2019). However, the effects of IMF stochasticity are clear when comparing the YCL across the three mass bins. The YCL is narrow, well defined, and roughly parallel to the reddening vector in the highest-mass bin. In the lowest-mass bin, the distribution is much broader and similar to the stochastic synthesis model predictions shown in Figure 2 of Fouesneau et al. (2012).

4.4. Quantitative Characterization

We now proceed to a quantitative characterization of the three principal features to facilitate further analysis. In particular, in Section 6, we will examine the spatial distribution of the populations associated with these features.

Our first step is to produce an uncertainty weighted color–color diagram. In Figure 10, each cluster is represented as a normalized Gaussian function with the color uncertainties adopted as standard deviations. Using this approach, clusters with low S/N color measurements are blurred out and do not provide high signal at their specific location in the diagram. On the other hand, more luminous clusters with more precise color–color measurements will dominate the distribution at their positions in these maps. Figure 7 shows that the color uncertainties are highest in regions that cannot be reached through reddening of the BC03 models. Uncertainties in the $V-I$ color are highest (left four panels) for clusters on the blue side of the BC03 model for middle-age clusters (100–500 Myr), and are particularly prominent for the ML sample. $U-B$ color uncertainties (bottom right panels) are highest redward of the BC03 model of old clusters (500 Myr–13.8 Gyr). By incorporating the uncertainty in the color–color diagrams in Figure 10, these regions with large photometric uncertainties are down-weighted and are less prominent as a result.

We provide definitions of the YCL, MAP, and OGC by selecting contour lines enclosing the respective regions. We define the MAP and YCL with contour lines enclosing 50% of all C1 clusters and C3 compact associations, respectively. To define the OGC, we select the largest contour lines of C1 clusters, which separates it from the MAP. We perform this analysis for the human- and ML-classified samples separately, as well as for the NUV-B versus $V-I$ diagram. The results are presented in Figures 10 and 11. Files providing these contours are at https://archive.stsci.edu/hlsp/phangs/phangs-cat.

Earlier in this section, we noted that the YCL appears roughly parallel to the reddening vector. The reddening vector corresponding to the Cardelli et al. (1989) reddening curve has a slope of 0.64 in the $U-B$ versus $V-I$ diagram. To probe the orientation of the YCL with respect to the reddening vector, we fit a straight line to the C3 compact associations, which are inside the 50% contour, and find a slope of 0.63 ± 0.01 and 0.814 ± 0.005 for the human and ML classifications, respectively. The general consistency for the human-classified C3 compact associations suggests that the shape of the C3 locus is indeed the result of the dust reddening of young clusters (for the ML sample, this is affected by the increased scatter due to IMF stochasticity). This exercise illustrates the potential of using color–color diagrams to test reddening laws using carefully selected young, dusty clusters and compact associations.

As discussed in Section 4.2, the human- and the ML-classified samples result in MAP distributions with the same

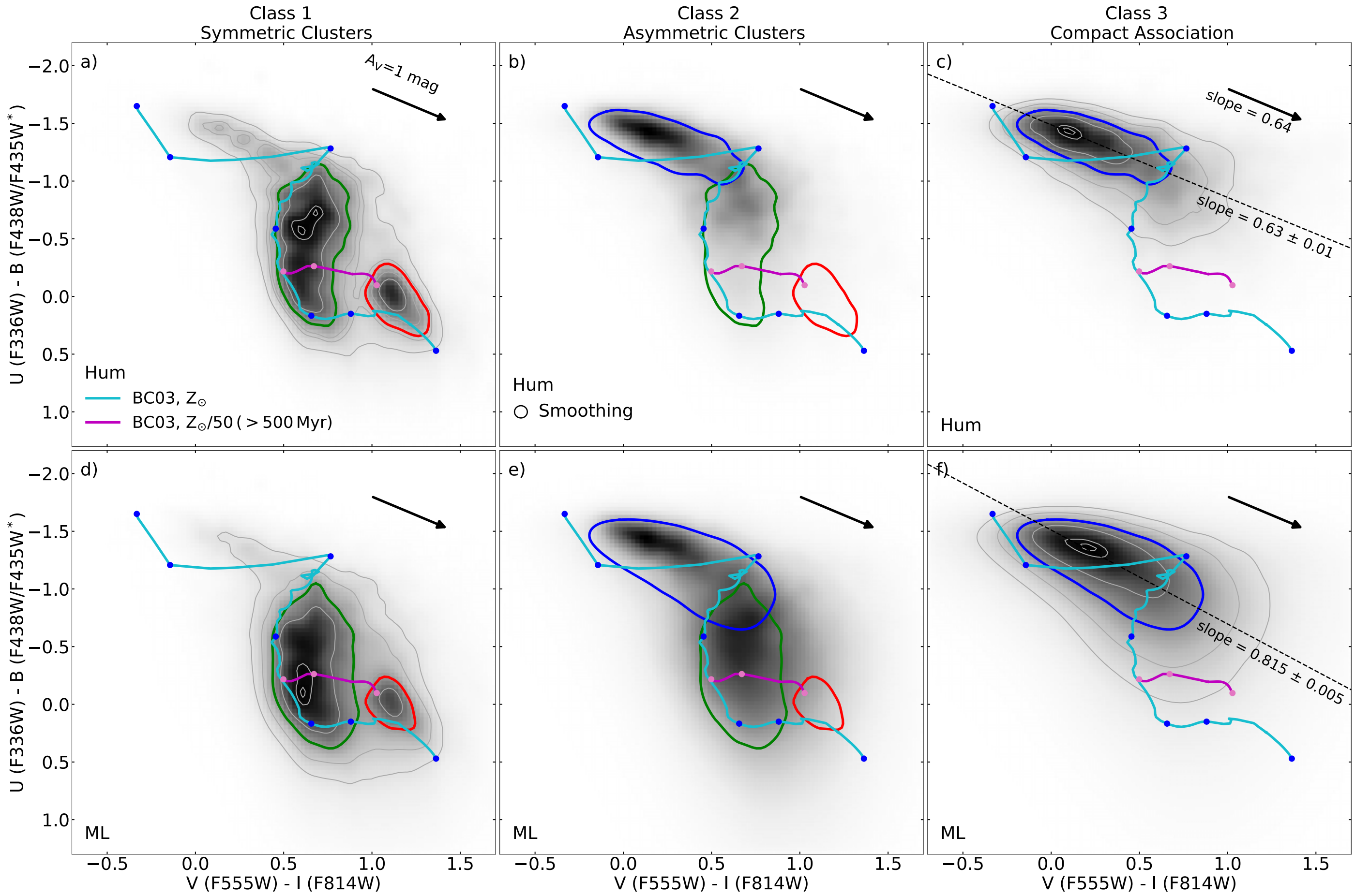

Figure 10. Characteristic regions in $U-B$ vs. $V-I$ color–color diagrams of C1 and C2 clusters and C3 compact associations. We show human- and ML-classified samples in the top and bottom row, respectively. We compute the color–color maps by stacking each cluster as a normalized Gaussian function on a grid using the color uncertainties as standard deviations. We then identify the YCL (blue) and the MAP (green) as the contour lines encircling 50% of the highest point for C1 clusters and C3 compact associations, respectively. We then find the largest contour line, which only encircles the OGC (red), separating this region from the MAP. We show the hulls of all three regions for C2 clusters. In order to compare the slope of the reddening vector and the sequence of dust-reddened objects in the YCL, we fit a linear function to all C3 compact association, which are inside the blue segmented area.

overall shape, but with a peak shifted toward redder (*U-B*) by ∼0.5 (i.e., implying older ages) for the ML sample, which appears to be due to its increased depth. Figures 10 and 11 show that the maximum of the MAP distribution for C1 clusters is located near an age of ∼100 Myr for the human-classified sample, whereas it is closer to an age of ∼400 Myr for the ML sample. There does not appear to be as clear of a difference in the peaks of the human- and ML-classified samples for the C2 clusters. When using the parameterization for these regions, one should keep in mind that, depending on whether the human or ML sample is used, populations of slightly different ages are represented.

5. Color–Color Diagrams: Individual Galaxies

Until this point, our analyses of the color–color diagrams have followed the approach of J. Lee et al. (2024, in preparation) and have been based on the cluster population aggregated across the full sample of PHANGS-HST galaxies. Here, we return to the more conventional approach of studying color–color diagrams for individual galaxies.

To provide a framework for analysis of the star cluster color–color distributions in the 38 individual galaxies (Figure 12), we consider the global SFR and stellar mass (M_*) of the galaxies, but now in the context of the star-forming galaxy MS (e.g., Lee et al. 2007; Noeske et al. 2007; Salim et al. 2007; Peng et al. 2010). As in Section 3.1, SFRs are based on an FUV+IR prescription, while the galaxy stellar masses are computed based on an IR flux and mass-to-light ratio.

To visualize trends in the star cluster color–color distributions with galactic star formation properties, in Figure 13, we plot the contours of individual color–color diagrams at the parent galaxy's position in the SFR–stellar mass (M_*) diagram. We compute ΔMS, the offset of the galaxy's position in the SFR–M_* diagram relative to the galaxy MS. We order the individual color–color diagrams in Figure 12 by ΔMS, from the most intensely star-forming galaxies farthest above the MS to those below the MS. Table 4 provides ΔMS and M_* for each galaxy. In these plots, we show only C1 and C2 clusters, which have a higher likelihood of being gravitationally bound.

To quantify changes in the relative distribution of clusters and associations among the three principal features of the color–color diagram, we compute the relative number fractions in the YCL, MAP, and OGC for each individual galaxy and examine them as a function of ΔMS (Figure 14). No attempt was made to correct for the variation in the depth of the YCL, MAP, and OGC populations due to evolution in the mass-to-

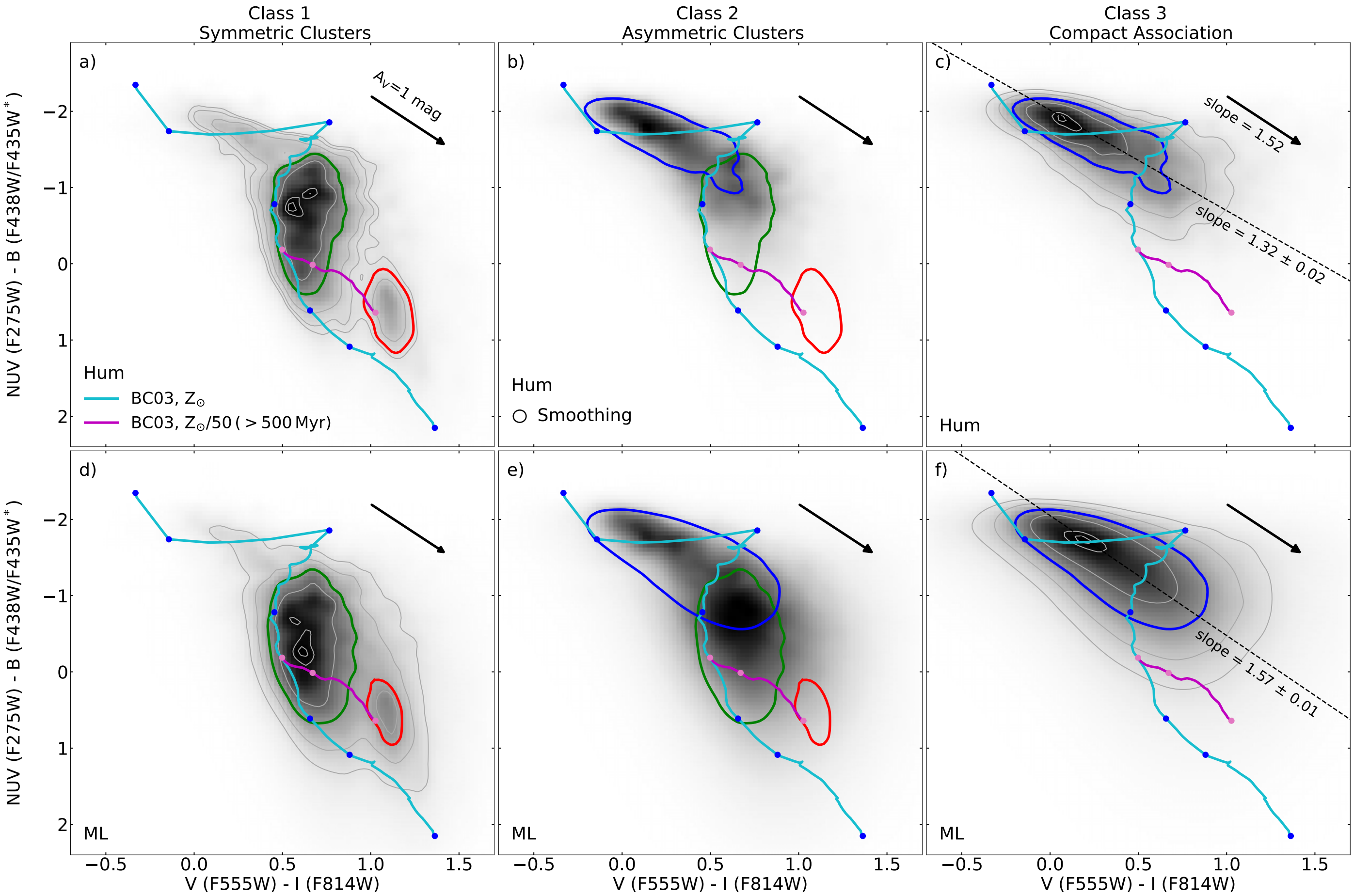

Figure 11. Same as Figure 10 but with NUV-B colors on the y-axis.

light ratio with age prior to computing these fractions. Thus, the absolute values of the number fractions themselves may not be physically meaningful. However, the general relative trends in Figure 14 should still provide insights into differences in the global processes that drive, regulate, and extinguish star and cluster formation across the galaxy sample. We also show that the differences in depth between the cluster samples for the different galaxies (e.g., due to distance) do not seem to affect the results.

5.1. *ΔMS and the Young Cluster Locus (YCL)*

Figure 14 shows no correlation between ΔMS and the relative number fraction of clusters associated with the YCL. There are at least two reasons for the lack of correlation. First, the dust-corrected FUV star formation indicator traces galaxy SFRs over ∼100 Myr timescales, while the YCL population is $\lesssim$10 Myr. Nevertheless, SFR tracers over these two timescales have been shown to correlate (e.g., Salim et al. 2007; Lee et al. 2009, and references therein). A more important issue involves the impact of dust on the observed colors of young clusters. An absent or weak YCL does not necessarily signify the lack of recent cluster formation. In fact, NGC 1365 and 1672, neither of which have a prominent YCL, have the largest ΔMS and are host to the most extreme central starbursts in the sample (Brandt et al. 1996; Querejeta et al. 2021; Whitmore et al. 2023b). These high sSFR galaxies have significant dust, which shifts the YCL feature along the reddening vector into the MAP (Paper II) and even into the OGC (Hollyhead et al. 2015). On the other hand, galaxies with low ΔMS values would be expected to have a lack of recent cluster formation, and a weak YCL. Examples of this are NGC 4826, and NGC 4569, which has the most peculiar color–color distribution of the sample. In this context, it is notable that NGC 4569 is the brightest late-type galaxy in the Virgo cluster. It experienced a ram pressure stripping event about 300 Myr ago (Vollmer et al. 2004; Crowl & Kenney 2008; Boselli et al. 2016), which drained the galaxy's gas reservoir and quenched its star formation. This event is reflected in the nearly complete absence of the YCL and unusual MAP in NGC 4569's cluster color–color diagram.

PHANGS-HST galaxies with prominent YCLs relative to the other color–color diagram features are NGC 7496, 1559, 4536, 1566, 1300, 685, and 2775. It is notable that, in their YCL regions, we mostly find C2 clusters, indicating that their asymmetric shape is associated with young age.

5.2. *ΔMS and Middle-age Plume (MAP)*

The MAP feature is visible for most of our galaxies, and for some galaxies, this feature is by far the most prominent one. Figure 13 shows that galaxies with more positive ΔMS values have more distinct MAP features. In fact, galaxies below the MS tend to lack this feature, as in NGC 4569, 4689, 4571, 1317, 4548, 2775, and 4826. This trend is apparent in Figure 14 through a clear correlation between the number fraction of clusters situated in the MAP and the ΔMS value.

A linear fit to this correlation yields the same slope of 0.14 for both human- and ML-classified cluster samples. This

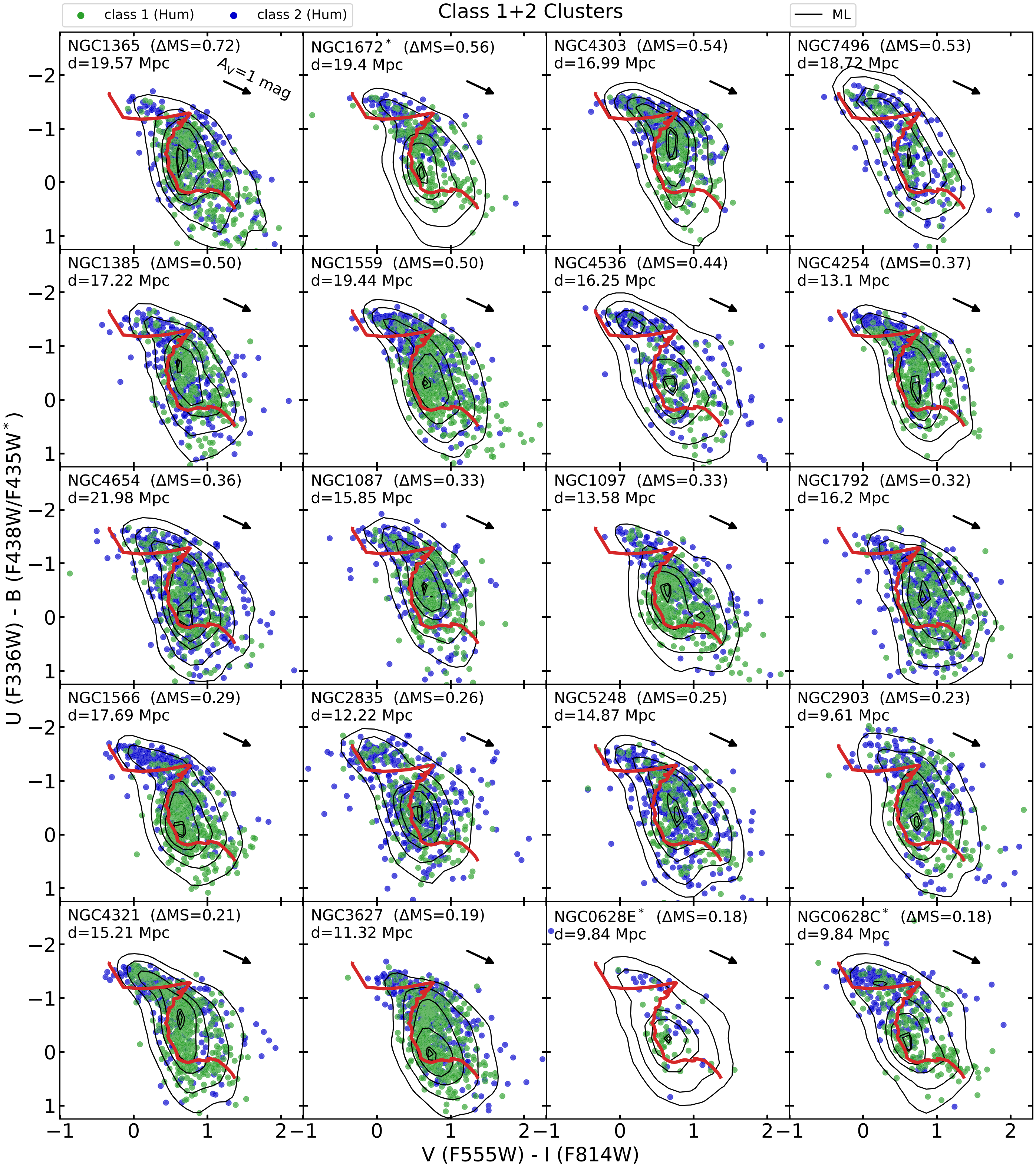

Figure 12. UBVI color–color diagrams for each individual PHANGS-HST galaxies. We present ML-classified class 1 and 2 clusters with black contours. With green and blue points, we overplot human-classified class 1 and 2 clusters, respectively. For reference, we show the solar metallicity track with a red line of the BC03 model. To indicate the direction of color–color shift due to reddening, we show a black arrow in the top left, which indicates a reddening of $A_V = 1$. To study the color–color distribution of each galaxy with respect to the position of the main sequence (MS) of star-forming galaxies (see Figure 13), we sort the diagrams in decreasing order of ΔMS values.

behavior may be expected since the SFR values are based on the UV emission and thus is an average of the star formation history over a few hundred Myr, and the MAP holds the largest fraction of such clusters.

It may be surprising that the correlations resulting from the human- and the ML-classified samples are the same given that the MAP distribution shows different peaks in color–color diagrams with the two samples. As discussed in Sections 4.2

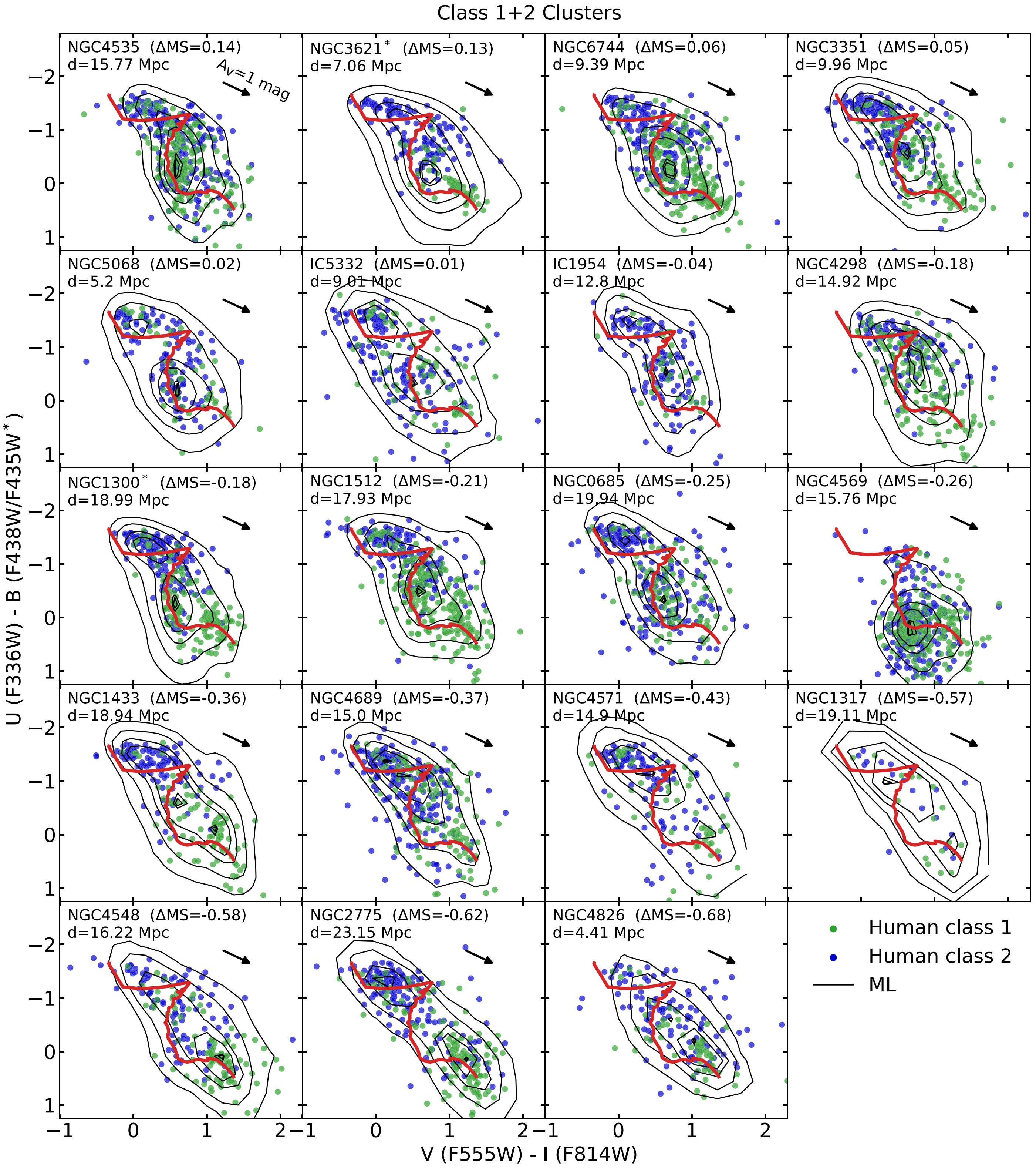

Figure 12. (Continued.)

and 4.4, the two peaks are separated by $(U-B)\sim 0.5$, which implies an age difference of a few hundred Myr. Despite this, there is no significant difference between the correlations in Figure 14. This could be due to the fact that the star (and cluster) formation rate should be relatively constant over a dynamical timescale for the galaxy, which happens to also be several hundred Myrs for spiral galaxies. We can estimate the the dynamical timescales as $\tau_{\rm dyn}\approx r/v_0$, where r is the galaxy radius, and v_0 is the asymptotic velocity of the modeled CO-rotation curves (Lang et al. 2020). The average for the PHANGS-HST galaxy sample is $\overline{\tau_{\rm dyn}} = 760$ Myr with the smallest measurement for NGC 1559 of $\tau_{\rm dyn} = 335$ Myr. If the

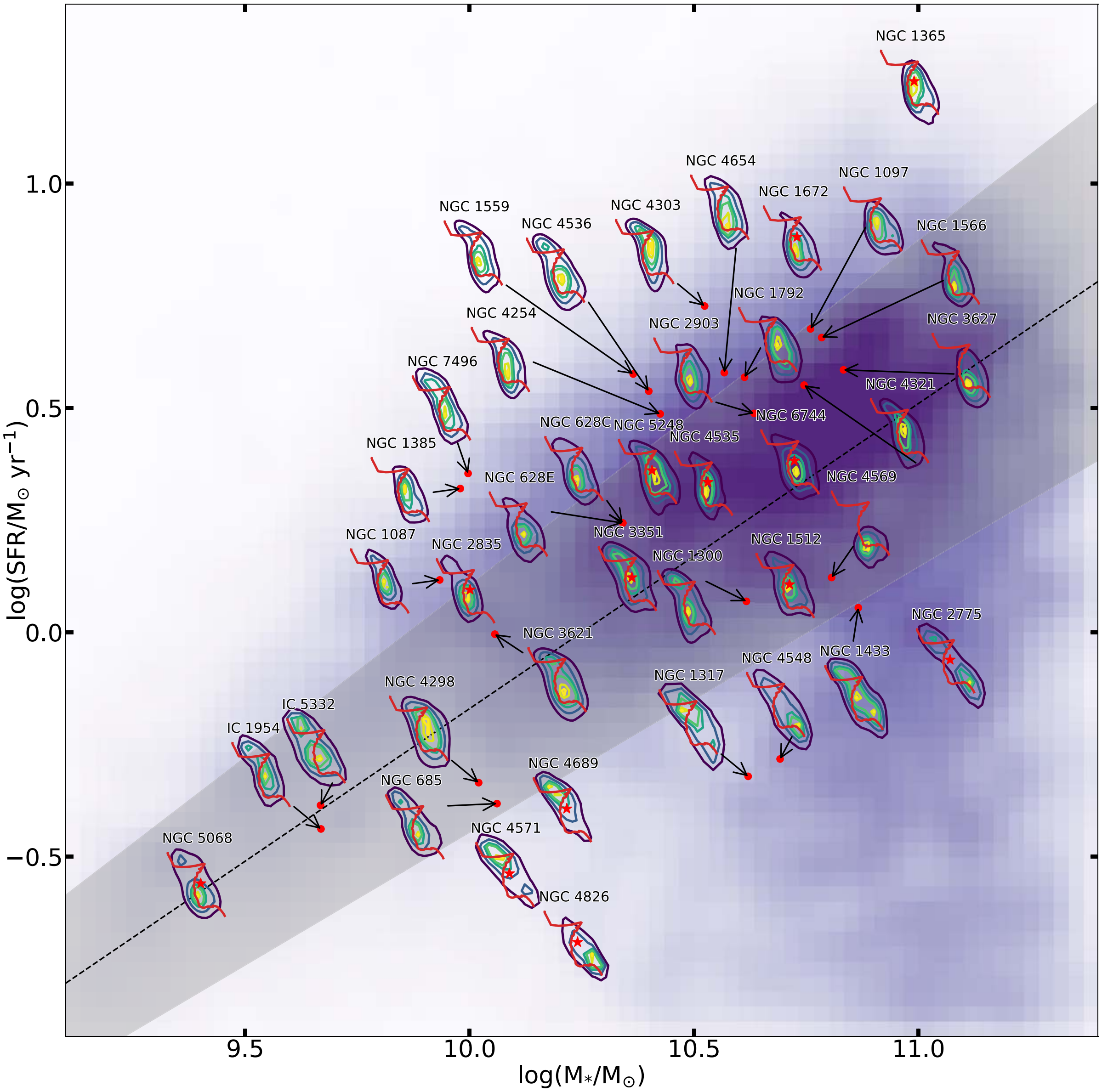

Figure 13. The main sequence (MS) of star-forming galaxies. We represent each galaxy of the PHANGS-HST sample as a $U-B$ vs. $V-I$ color–color diagram (Figure 12) at the position on the MS of their host galaxy. The color–color diagrams are presented by contours computed for the ML catalog of C1 and C2 clusters. As a reference, we show for each diagram the BC03-model track in red. For crowded regions, we shift the color–color diagrams and denote their position on the MS with a red point and an arrow. For those galaxies that are not in a crowded region, we mark their position on the MS with a red star, situated in the center of the color–color diagrams. The purple background represents the density of SDSS galaxies of $z < 0.2$ with M_* and SFR values computed by Salim et al. (2016). The dashed line is the predicted MS at $z = 0$ defined by Leroy et al. (2021), and the gray area shows the standard deviation computed by Catinella et al. (2018). The essence of this figure is the connection between star formation activity and the cluster population of all PHANGS-HST galaxies. As discussed in the text, the star formation rates are sensitive to timescales of $<$100 Myr, and therefore, the relative fractions of MAP clusters correlate with the relative position on the MS as shown in Figure 14.

dynamical timescales of the galaxies in the sample were shorter (e.g., for dwarf galaxies), a difference in depths of the samples would more likely affect the results.

To further investigate cluster sample completeness issues that may influence the relative fraction of clusters in the MAP, we tested for correlations with the galaxy distance (Figure 16). There is no correlation with the distance. There is also no correlation with the median absolute V-band magnitude M_V of the cluster sample. The lack of correlation between the cluster sample depth and the fraction of MAP clusters is most likely explained by the fact that we are computing the relative fraction of these cluster groups and not the total numbers. This suggests that the relative fractions are not sensitive to the variation in depth, which is described in Section 3.2, and which spans over ∼1 mag in the V band.

5.3. ΔMS and Old Globular Cluster Clump (OGC)

The OGC feature in the color–color diagram contains the oldest star cluster populations in each galaxy. A larger relative number of globular clusters may indicate intense star formation in the early evolutionary phase of the galaxy (Brodie & Strader 2006), whether in situ or ex situ (Choksi & Gnedin 2019, and references therein), but also means that the clusters have not been disrupted and have persisted through time. In particular, NGC 4826, 6744, 3621, 628 c, 1097, 1512, 1433, 1300, and

Table 4
Tabular Representation of Dependence between ΔMS and Galaxy Morphological Properties

ΔMS	log M_*	Morphological Features						
(dex)	($M_\odot$)	Bar-driven SF[a]	Central Ring	SF End of Bar[b]	Global Arms[c]	Bulge[d]	Flocculent[e]	Quiescent[f]
0.72	10.99	N1365	N1365	N1365	N1365	⋯	⋯	⋯
0.56	10.73	N1672	N1672	N1672	⋯	⋯	⋯	⋯
0.54	10.52	N4303	⋯	N4303	⋯	⋯	⋯	⋯
0.53	10.00	N7496	⋯	N7496	⋯	⋯	⋯	⋯
0.50	9.98	N1385	⋯	⋯	N1385	⋯	N1385	⋯
0.50	10.36	N1559	⋯	⋯	N1559	⋯	⋯	⋯
0.44	10.40	⋯	⋯	N4536	⋯	⋯	⋯	⋯
0.37	10.42	⋯	⋯	⋯	⋯	⋯	⋯	⋯
0.36	10.57	N4654	⋯	N4654	N4654	⋯	⋯	⋯
0.33	9.93	⋯	⋯	⋯	⋯	⋯	N1087	⋯
0.33	10.76	N1097	N1097	N1097	⋯	⋯	⋯	⋯
0.32	10.61	⋯	⋯	⋯	⋯	N1792	⋯	⋯
0.29	10.78	⋯	⋯	⋯	N1566	N1566	⋯	⋯
0.26	10.00	⋯	⋯	⋯	N2835	⋯	⋯	⋯
0.25	10.41	⋯	⋯	⋯	N5248	⋯	⋯	⋯
0.23	10.63	N2903	⋯	N2903	⋯	⋯	⋯	⋯
0.21	10.75	⋯	N4321	⋯	N4321	⋯	⋯	⋯
0.19	10.83	N3627	⋯	N3627	N3627	N3627	⋯	⋯
0.18	10.34	⋯	⋯	⋯	N628	N628	⋯	⋯
0.14	10.53	N4535	⋯	⋯	N4535	⋯	⋯	⋯
0.13	10.06	⋯	⋯	⋯	⋯	N3621	N3621	⋯
0.06	10.72	⋯	⋯	⋯	⋯	N6744	N6744	⋯
0.05	10.36	N3351	N3351	⋯	⋯	N3351	N3351	⋯
0.02	9.40	⋯	⋯	⋯	⋯	⋯	N5068	⋯
0.01	9.67	⋯	⋯	⋯	⋯	⋯	I5332	⋯
-0.04	9.67	⋯	⋯	⋯	I1954	⋯	⋯	⋯
-0.18	10.02	⋯	⋯	⋯	⋯	⋯	N4298	⋯
-0.18	10.62	N1300	N1300	N1300	N1300	N1300	⋯	⋯
-0.21	10.71	N1512	N1512	N1512	⋯	N1512	N1512	⋯
-0.25	10.06	⋯	⋯	⋯	⋯	⋯	N685	⋯
-0.26	10.81	N4569	⋯	N4569	⋯	⋯	⋯	N4569
-0.36	10.87	⋯	⋯	⋯	⋯	⋯	N1433	⋯
-0.37	10.22	⋯	⋯	⋯	⋯	⋯	N4689	⋯
-0.43	10.09	⋯	⋯	⋯	⋯	⋯	N4571	⋯
-0.57	10.62	⋯	⋯	⋯	⋯	⋯	N1317	⋯
-0.58	10.69	⋯	⋯	N4548	⋯	N4548	⋯	⋯
-0.62	11.07	⋯	⋯	⋯	⋯	N2775	N2775	N2775
-0.68	10.24	⋯	⋯	⋯	⋯	N4826	⋯	N4826

Notes. PHANGS-HST galaxies are sorted in order of decreasing MS deviation, and the NGC/IC number is shown in the following columns whenever the specified column property is applicable to a particular galaxy. The galaxy stellar mass is also provided.

[a] Bar-driven SF: i.e., short bars (like NGC 4536 and NGC 685) and stellar bars with minimal star formation (e.g., NGC 6744, and NGC 4548) are not included, since they do not appear to be generating much star formation.

[b] SF End of Bar: a clear enhancement of star formation at the end of the bar (like NGC 1300) compared to downstream.

[c] Global Arms: relatively continuous star formation along the spiral arm for at least 180° (like NGC 1566 and NGC 4535).

[d] Bulge: Evidence of an old (red), roughly spherical or slightly flattened central component without extensive star formation (e.g., NGC 3351, NGC 2775). Generally associated with the presence of old globular clusters.

[e] Flocculent: Rather than global arms, star formation is in short, irregular regions of star formation. See Elmegreen & Elmegreen (1987).

[f] Quiescent: Large regions without active star formation. Often associated with galaxies that have had their gas removed by ram pressure stripping (e.g., NGC 4689; Kenney & Young 1986).

(This table is available in machine-readable form.)

2775 host a significant population of old globular clusters, which are almost exclusively classified as C1. There is no correlation with ΔMS.

6. An Atlas of Star Cluster Spatial Distributions

A careful examination of Figure 13 in combination with our HST imaging reveals a number of trends between the positions of the galaxies in the diagram and galaxy morphology. This motivates examination of the properties of the cluster populations in relation to both ΔMS and galaxy morphology. For this and other science applications (e.g., calculation of correlation functions, constraints on star formation timescales, and comparison with simulations, e.g., Gouliermis et al. 2014; Grasha et al. 2015, 2017, 2019; Turner et al. 2022), it essential to examine the 2D spatial distribution of clusters in each galaxy.

Here, we provide an atlas of star cluster maps for the full PHANGS-HST 38 galaxy sample. In Figure 17, we present the

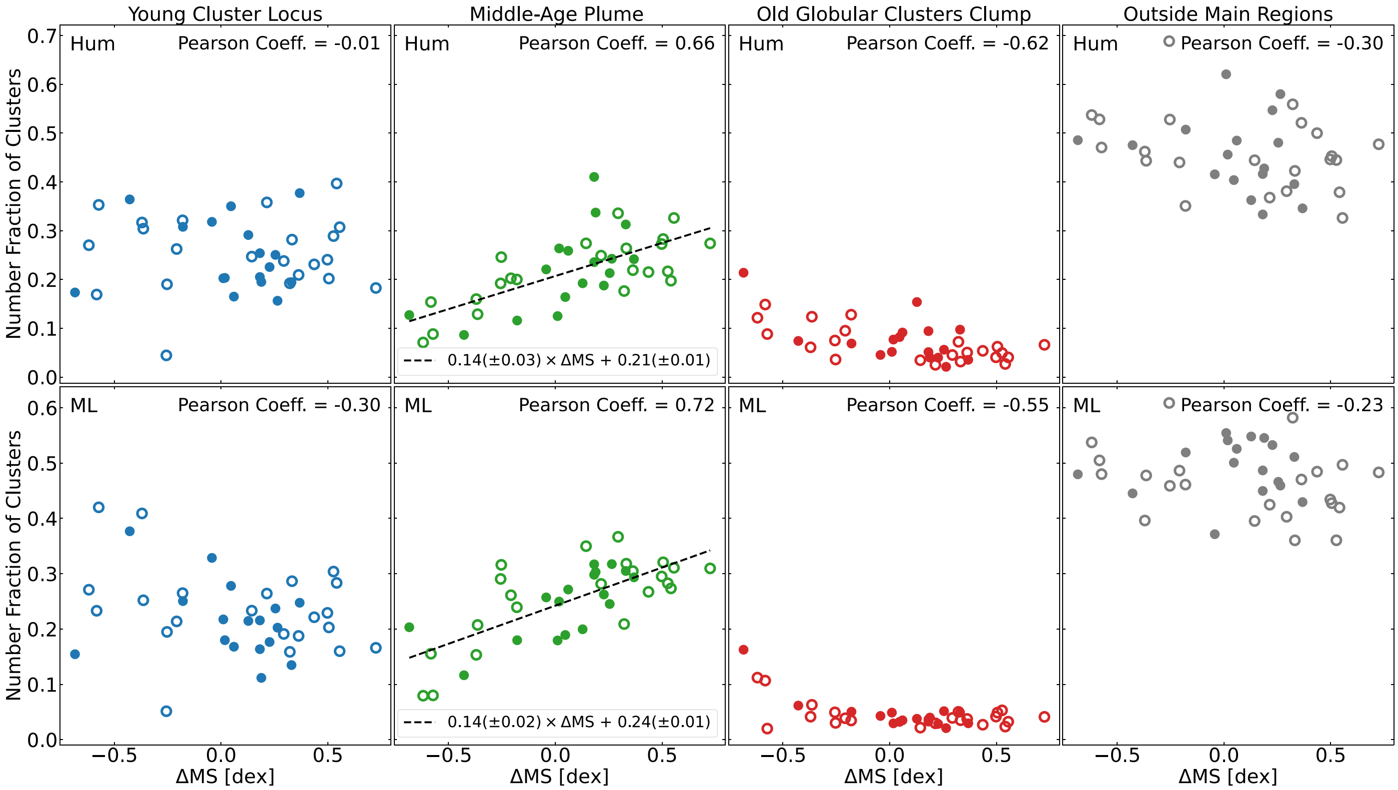

Figure 14. Number fraction of C1 and C2 clusters of each galaxy associated with the main characteristic regions in color–color diagrams found in Section 4.4 as a function of ΔMS. We show the YCL, the MAP, and the OGC in blue, green, and red, respectively. In gray, we show clusters outside the main regions. We distinguish galaxies at a distance of smaller and larger than 15 Mpc with full and open circles respectively. For each panel, we show the Pearson correlation coefficient in the top right. Since the MAP shows a strong correlation, which we explain in the text, we fitted a linear function to the data points and provide the fit parameters.

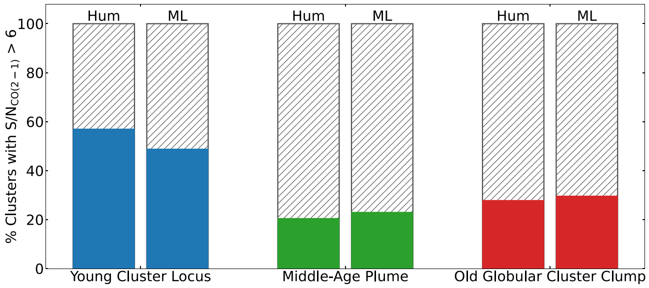

Figure 15. Histograms representing the percentage of C1 + C2 compact clusters associated with molecular clouds. We show for each characteristic region (YCL, MAP, and OGCC) the percentages of clusters that are cospatial with ALMA CO(2-1) molecular gas detection with an $S/N > 6$. The human-classified and machine-learning-classified samples are shown separately.

spatial distributions of the clusters associated with the three principal features of the color–color diagram—the OGC, MAP, and YCL. A color-composite HST image is included, and ALMA CO(2-1) intensity contours are overlaid on the maps of the YCL. Following the analysis of the previous section, we show the maps in decreasing order of ΔMS values.

A broad examination of the overall atlas shows that objects associated with the YCL are generally found in areas with CO, as expected. On average, we find that YCL objects are coincident with CO twice as often as objects associated with the MAP or OGC (Figure 15). As also expected, YCL objects closely trace the spiral structure and central dynamical rings, and reflect the structure of the ISM from which they are born. These structures then disperse with age—the spatial organization is broader for the MAP objects, and is closest to a random distribution for objects associated with OGC.

7. Galaxy Morphology

To facilitate a multiscale examination of trends across the 38 PHANGS-HST galaxies, we combine information about key galaxy morphological features with galaxy M_* and ΔMS in Table 4. The classifications in Table 4 are based on a visual examination of a BVI image by co-author B.C.W.

We have checked how well our visual classifications agree with prior reference studies in the literature for bars, global spiral structure, and flocculent star formation. For example, we find that all 15 galaxies in which we have identified bar-driven SF (i.e., either in the bar, in a central star-forming ring at the inner end of the bar, or at the outer end of the bar) are indeed classified as barred (11/15 as SB and 4/15 as SAB) by Buta et al. (2015).

We performed a similar check on our classification of spiral structure, as determined by Elmegreen & Elmegreen (1987). Here, we find that eight of the nine galaxies in which we have identified global spiral structure, and that are within the sample defined by Elmegreen & Elmegreen (1987), are consistent with their determinations. Similarly, nine of the 11 galaxies in common, characterized as flocculent, agree. We conclude that our classifications are in reasonably good agreement with previously established determinations.

Starting at the top of Figure 13 and Table 4, we note that several of the galaxies with the largest positive residuals are galaxies with star-forming bars, such as NGC 1365, NGC 1672, NGC 4303, NGC 7496, NGC 1385, and NGC 1559. On the other hand, most of the galaxies with the largest negative residuals are flocculent and quiescent galaxies, like NGC 4826, NGC 2775, NGC 4548, NGC 1317, NGC 4571, and NGC

4698. Other properties that tend to be correlated with positive ΔMS are the presence of star formation at the end of the bars and the presence of global spiral arms. Galaxies with bulges tend to have negative ΔMS as expected.

8. Relation of Cluster Population Properties to ΔMS and Galaxy Morphology

8.1. Bars and Central Rings

As just mentioned, many of the galaxies with the largest ΔMS are those with bars that appear to be driving star formation. The presence of a strong bar is known to effectively funnel gas into the galaxy's central regions (e.g., Athanassoula 1992; Sellwood & Wilkinson 1993; Kuno et al. 2007; Schinnerer et al. 2023; Sormani et al. 2023). This process creates high gas densities, leads to more efficient star formation, and often promotes cluster formation.

An examination of the star cluster color–color diagrams for such galaxies in Figure 12 shows they all have prominent MAPs, as expected based on Figure 14. NGC 1365, the galaxy with the highest SFR in the sample (16.90 $M_\odot$ yr^{-1}), is exceptional, and this activity results from the combination of a bar that drives a central star-forming ring, and strong spiral arm structure. It not only has a particularly prominent MAP but also has the richest population of massive young clusters of any known galaxy within 30 Mpc, with ~30 star clusters more massive than $10^6 M_\odot$ and younger than 10 Myr (Whitmore et al. 2023b).

The cluster spatial distribution maps (Figure 17) reveal star formation hotspots where young clusters dominate, many of which are related to the presence of a bar. Beyond NGC 1365, central star-forming rings are found in an additional six galaxies, and all but one of these galaxies also exhibit a clear bar morphology (Table 4). The presence of the ring is reflected in the distribution of young star clusters. Concentrations of young clusters also appear at the connection points between bars and spiral arms as observed in NGC 1365, 7496, 1097, 1300, and 1512. The enhanced star formation at these parts of galaxies is explained by the increase of density due to the elliptical orbits in bars (e.g., Nguyen Luong et al. 2011; Beuther et al. 2017; Sormani et al. 2020; Tress et al. 2020; Levy et al. 2022). Interestingly, these cluster hotspots are dominated by highly dust-reddened ($>1.5 A_V$) young (<10 Myr) clusters, which are located in the MAP or globular cluster region rather than the YCL (Whitmore et al. 2023a; Paper II). This means that these high density regions have large amounts of dust, which have a major impact on our HST UV–optical observations, and long-wavelength JWST and ALMA observations become essential for studying the earliest stages of dust and embedded star and cluster formation (e.g., Johnson et al. 2015; Emig et al. 2020; Rico-Villas et al. 2020; Costa et al. 2021; Leroy et al. 2021; Levy et al. 2021, 2022; Whitmore et al. 2023b; Linden et al. 2023; Schinnerer et al. 2023; Sun et al. 2024).

Another common feature of galaxies with bar-driven star formation is that middle-age clusters are found near the young cluster hotspots, as well as throughout the bar (e.g., NGC 1672, NGC 2903, NGC 1097). A comparison with the distribution of the old globular clusters, which are more uniformly distributed, makes it clear that the middle-age clusters still reflect the dynamical features of their galaxy.

Some galaxies show a string of middle-age clusters parallel to the bar (e.g., NGC 1097). This population seems to be a relic from a star formation episode after which the star clusters remained on a similar orbit. In fact, this scenario is described by simulations in Dobbs & Pringle (2010), and their Figure 2 reflects a situation where ~50 Myr old clusters are orbiting parallel to the bar. Sormani et al. (2020) suggested that such clusters are formed near the central ring and then collectively moved out into the galaxy. Considering the relative position above the MS of these galaxies, we can infer that such a past star formation episode contributes to the enhanced SFR value.

8.2. Flocculent Star Formation

Galaxies with flocculent morphologies dominate the galaxies below the MS (i.e., with negative ΔMS; see Table 4). As already discussed in Section 5.2 and shown in Figure 14, galaxies with negative ΔMS tend to have peculiar color–color diagrams (Figure 13), which lack a distinct MAP feature, indicating a major departure from steady-state star formation due to interactions with their external environments.

An examination of individual cases shows the connection between the MAP deficiency, and galaxy morphology. In particular, NGC 2775 is of Type a SA(r)ab with an intermediate sized bulge, a flocculent disk, and a color–color distribution that appears strongly bimodal. It has the second lowest ΔMS in the sample and flocculent structure so striking that its HST imaging has captured broad attention.[48] Almost all C1 clusters are situated in the bulge, and C2 clusters are in the disk (Figure 17). The bimodal distribution originates from the combination of a relatively dust free old central region with no recent star formation (Hogg et al. 2001), and flocculent star formation thought to be seeded by accreted gas (i.e., from the nearby companion NGC 2777, Arp & Sulentic 1991), which led to a disk rejuvenation event.

Two other flocculent galaxies NGC 4571 (Kennicutt 1983) and NGC 4689 (Elmegreen et al. 2002) exhibit a strong YCL feature. They are adjacent in Figure 13 below the MS. NGC 4689 is a member of the Virgo cluster. The galaxies are not able to sustain their star formation as they are presumed to have lost most of their gas due to their environment (Kenney & Young 1986), resulting in a weak MAP.

Our multiscale observational analysis is consistent with a two-component disk model, which predicts a dearth of intermediate age stars in the disk of a flocculent galaxy (Elmegreen & Thomasson 1993; Sellwood & Masters 2022). In this model, flocculent patterns arise through gravitational instabilities in a low-mass cool disk component embedded in a massive halo. Sellwood & Masters (2022) suggest that a two-component disk could arise naturally with the abrupt accretion of gas following a period of gas starvation. Flocculent instabilities would then give rise to star formation in short arm segments.

All of these flocculent galaxies below the MS show an evenly distributed cluster population with no significant hotspots of clusters.

9. Discussion

With the completion of the largest HST census to date of star clusters and compact associations, we are beginning to realize

---

[48] https://esahubble.org/images/potw2026a/

the scientific potential of PHANGS-HST to build upon the previous generation of star cluster studies (e.g., Portegies Zwart et al. 2010; Renaud 2018; Krumholz et al. 2019; Adamo et al. 2020, and references therein), and break new ground in the multiscale characterization of their observational properties.

The nature and size of our data set allow us to bring together once-separate techniques for the characterization of galaxies (galaxy morphology and location relative to the galaxy MS) and clusters (color–color diagrams and 2D spatial distributions) for a diverse sample of spiral galaxies. We provide a broad overview of the demographics of the objects in our catalogs, which demonstrates that tremendous insight can be gained from the observed properties of clusters alone, irrespective of the exact choice of model SSP track, and even in the absence of their transformation into physical quantities.

In particular, we show how the PHANGS-HST cluster sample greatly expands the utility of the color–color diagram. In particular, the UBVI CCD reveals that the three standard morphological classes of clusters and associations map to distinct combinations of YCL, MAP, and OCG features, and hence to distinct age distributions. It provides a model-independent graphical representation of both the star formation history of individual galaxies as traced by clusters, as well as the cosmic cluster formation history of disk galaxies. When coupled with population synthesis model tracks and dust reddening laws, the UBVI CCD is important for not only testing SSP models (e.g., Maraston 1998; Larsen & Richtler 1999; Bruzual & Charlot 2003; Vázquez & Leitherer 2005) but also exposing the uncertainties in the translation of photometric colors into ages, and specific degeneracies between age and reddening. The much broader distribution of low luminosity/low-mass systems in the UBVI CCD confirms how photometric colors do not map uniquely to a given age for this population, even if the reddening and metallicity are known, due to the stochasticity in the presence of massive stars and short-lived stellar evolutionary phases (e.g., Fouesneau & Lançon 2010; Silva-Villa & Larsen 2011; de Meulenaer et al. 2013; Krumholz et al. 2015; Orozco-Duarte et al. 2022).

Of course, when comparing the photometric properties to model predictions, it is important to understand the accuracy of the model and its limitations. Throughout the paper, a BC03 SSP solar metallicity model is shown to provide context for discussion of the distribution of the cluster population in color–color diagrams, but there are apparent inconsistencies between this track and the observed color distribution as noted in our previous papers (e.g., Turner et al. 2021; Deger et al. 2022). For example, the color evolution of the model between 3 and 5 Myr is too blue in $V-I$ and/or too red in $U-B$ by a few tenths relative to the observed YCL (even accounting for the impact of dust along the reddening vector). The sharp turn to the red at 5 Myr in NUV-BVI and UBVI does not seem to be reproduced by the shape and position of the YCL. There appears to be an inconsistency between the relative position of YCL and MAP and tracks in the BVI compared with that in the UBVI diagrams. The track does not incorporate nebular emission, which would produce a red "hook" for ages <3 Myr, which would be important for some fraction of the youngest clusters. These complications are one motivation for the focus on the observed properties of our sample in this paper, which are far more likely to stand the test of time.

Clearly, a great deal of work lies ahead to use this sample to test and constrain SSP models (e.g., Wofford et al. 2016, and references therein), and this will be the focus of upcoming work. A quantitative determination of ages, reddenings, and stellar masses through SED fitting assuming the BC03 SSP model track is presented in Paper II. A proper quantitative study of the timescales and processes governing the star and cluster formation cycle requires a robust determination of these physical properties, a clear understanding of underlying model uncertainties, together with a proper determination of completeness limits of the catalogs. In the remainder of this section, we discuss issues related to sample completeness both to outline future work and to provide advice to users of the catalog.

Characterizing the completeness of star cluster samples is known to be a messy business. While the completeness will depend on the distance of the galaxy (which changes by a factor of 4 from 5 to 23 Mpc in PHANGS-HST), it also is affected by the following:

1. *Local background in the galaxy, which can be highly variable*. For example, cluster candidates are not detected in the bright central regions of some galaxies (e.g., NGC 1566, 3627, 1317, and 4548; Figure 17 and the online figure set). The completeness will also be a function of the density of resolved sources (crowding).
2. *Dust, which can also be highly variable across a galaxy*. The incompleteness will be higher for the youngest clusters ($\lesssim$5 Myr), which are still clearing the natal gas and dust from the environments in which they are born. The earliest stages of star and cluster formation will be entirely dust enshrouded and unobservable in the optical. The PHANGS-JWST data set will be critical in this regard for completing the cluster census at young ages, and this was a key science driver for the survey (Lee et al. 2023, and references therein).
3. *The size of the cluster, and the underlying cluster size distribution*. The incompleteness is likely higher for the most compact clusters, which may not be distinguishable from a point source (e.g., Ryon et al. 2017; Brown & Gnedin 2021).
4. *The details of the source detection algorithm and candidate selection criteria*. Two issues are particularly important to note in this context.
5. *The age of the cluster, due to the evolution of the mass-to-light ratio*.
    (a) As discussed in Lee et al. (2022) and Section 2.4, the PHANGS-HST pipeline is optimized to identify single-peaked clusters, which leads to a high level of incompleteness for multipeaked stellar associations (C3). The majority of star formation occurs in stellar associations (Lada & Lada 2003; Ward & Kruijssen 2018; Ward et al. 2020; Wright 2020, and references therein). Whether the C3 compact associations provided in this catalog should be used will thus be heavily dependent on the science goal of the analysis. A separate pipeline for stellar associations, based on a watershed algorithm, provides a far more complete inventory of young stellar populations across multiple physical scales (Larson et al. 2023). Multiscale stellar association data products for the full 38 PHANGS-HST galaxy sample will be published at a later date.
    (b) Even when pipelines are specifically developed for single-peaked clusters, differences in the adopted detection algorithm and morphological selection

criteria (which has generally been based on some form of concentration index, e.g., Chandar et al. 2010; Adamo et al. 2017) can lead to significant differences in the populations captured. As discussed in Thilker et al. (2022), LEGUS (Calzetti et al. 2015) has produced cluster catalogs for four of the seven galaxies in common with PHANGS (NGC 628, NGC 1433, NGC 1566, NGC 3351),[49] and there is an overlap of 50%–75% of human verified C1 and C2 clusters in the union of the LEGUS+PHANGS-HST catalogs. Understanding the differences in the catalogs, and comparison of results based on the union of the two catalogs with those based on the separate catalogs from each survey will be important subjects for future investigations.

6. *Unknown–unknowns, e.g., systematics in the neural network morphological classifications.* This is particularly for the fainter sources in the sample for which human classifications were not generally performed.

In the future, an analysis of artificial star clusters added to the HST imaging can be performed to quantify catalog completeness (e.g., Adamo et al. 2017; Tang et al. 2023). In the meantime, we present the following:

1. In Section 3, we provide basic statistics for the size and depths of the catalogs for both individual galaxies and the total sample aggregated across all 38 galaxies. These data can be used to estimate the completeness limit of the catalogs, by locating the turnover point in the luminosity (or mass functions) as has been done in prior work (e.g., Mayya et al. 2008; Ryon et al. 2017; Cook et al. 2019; Cuevas-Otahola et al. 2023).
2. An analysis can be conducted using different subsamples of the catalog, selected based on a completeness-dependent parameter, and the results compared. For example, subsamples can be defined with different magnitude limits, galaxy distances, from different regions of the galaxies (e.g., excluding the inner crowded, high background parts of the galaxy). A comparative analysis using C1 versus C2 versus C1+C2 samples, as suggested in Whitmore et al. (2021) and demonstrated in several figures in the current paper (e.g., Figures 6 and 8), can also be performed.

Finally, due to the black-box nature of the neural network models, a comparative analysis with human-classified and machine-classified catalogs should be performed. It would be hoped that the agreement between human and ML classification would be so robust that we can rely entirely on the ML catalog once it is built. While the current state of the art is quite promising (especially for C1+C2), we are not yet at a stage where ML classification can be used blindly—care must be taken. ML classifications will continue to improve, but the subject is still at an early stage of development. See Wei et al. (2020), Pérez et al. (2021), Whitmore et al. (2021), and Hannon et al. (2023) for additional discussion and other examples of how well the ML classifications perform for specific science applications.

10. Summary

We present the largest catalog of star clusters and associations to date for nearby galaxies. For the 38 spiral galaxies of the PHANGS-HST survey, which span distances between 5 and 23 Mpc, our catalog provides aperture-corrected photometry in the NUV-*U*-*B*-*V*-*I* filters for the following:

1. A total of ∼20,000 star clusters and compact associations, with a median of ∼500 sources per galaxy, have been visually inspected and morphologically classified by a human (co-author B.C.W., Whitmore et al. 2021). This subset of the catalog is comprised of ∼8000 C1 and ∼8000 C2 clusters, and ∼6000 compact associations (C3). The median m_V of this human-classified sample is ∼–8 mag (Vega).
2. A larger sample of ∼100,000, with a median of ∼1700 sources per galaxy, has passed neural network classification (Hannon et al. 2023). This sample is comprised of ∼13,000 C1 and ∼23,000 C2 clusters, and ∼60,000 compact associations (C3). The neural network models were trained on the human-classified sample, and deployed on the entire cluster candidate list of ∼190,000 sources. This yields a sample of clusters and associations ∼1 *V*-band magnitude deeper than the human-classified sample.

We provide a broad overview of the observed properties of the photometric catalogs. A summary of our findings is as follows.

Regarding UV–optical color–color diagrams for star clusters and associations.

1. Given the typical depth of HST Treasury surveys of nearby galaxies with the WFC3 camera, the *U*-*B*-*V*-*I* color–color diagram provides the greatest diagnostic power (relative to *B*-*V*-*I* and NUV-*B*-*V*-*I*) for distinguishing between different age populations and separating its three principal features— the YCL ($\lesssim$ 10 Myr), the MAP (1 Gyr $\lesssim t \lesssim$ 100 Myr), and the OGC ($t \gtrsim$ 1 Gyr; Section 4.1). We provide contour based definitions for each feature (Section 4.4).
2. We study the observed properties of the cluster population on the color–color diagram combined across all 38 spiral galaxies in the PHANGS-HST survey. This shows that the C1, C2, C3 morphological classes each have distinct color–color diagrams, and hence map to distinct age distributions. C1 clusters have a prominent MAP and OGC, and weak, but narrow YCL. C2 clusters have a clear YCL and MAP, but no OGC. C3 compact associations have a strong YCL, and no significant MAP or OGC. In particular, the large sample demonstrates that the properties of C1 and C2 clusters are distinguishable (Section 4.1).
3. The differences in the YCL, MAP, and OGC features indicate that age distributions skew younger as the degree of cluster asymmetry and central concentration increases from C1 to C3, and are consistent with the expectation that the process of cluster dissolution should yield some correlation between age and morphology (e.g., Adamo et al. 2017; Whitmore et al. 2021; Cook et al. 2023, and references therein; Section 4.1).
4. The distribution of clusters in the color–color diagram is qualitatively similar for human- and ML-classified

---

[49] https://archive.stsci.edu/prepds/legus/dataproducts-public.html

clusters when both samples have similar magnitude limits. This provides evidence for the robustness of the ML classifications (Section 4.2).

5. The distribution of low-mass young clusters ($<5000\ M_{\odot}$) on the color–color diagram shows increased scatter, which is generally consistent the impact of stochastic sampling of the stellar IMF (Section 4.3).

We bring together various techniques—the characterization of galaxies (galaxy morphology and location relative to the galaxy MS) and cluster populations (color–color diagrams and 2D spatial distributions)—to explore the data set in a multiscale context and demonstrate that the UBVI color–color diagram is a highly valuable, model-independent, observational diagnostic of the star and cluster formation history and evolutionary status of the galaxy.

1. As expected, YCL populations closely trace spiral structure. They are coincident with CO twice as often as objects associated with the MAP or OGC, and reflect the structure of the ISM from which they were born. These structures then disperse with age as has been found previously—the spatial organization is broader for the MAP objects, and is closest to a random distribution for objects associated with OGC (Section 6).
2. There is no correlation between ΔMS and the fraction of clusters in the YCL. The absence of a strong YCL feature at above the MS is generally due to dust reddening and does not necessarily imply the absence of cluster formation. Above the MS, strong bars, a number of which are associated with central star-forming rings, appear to be driving high star formation densities and promote cluster formation. Clusters trace the star-forming rings, concentrations of clusters appear at the bar ends, and these populations tend to be highly dust reddened. At low ΔMS, the relative fractions of the cluster populations in each of the features reflect a complex star formation history due to the external environment of the galaxy (e.g., Virgo cluster) and interactions with neighboring galaxies. At low ΔMS, many galaxies have flocculent morphologies and evidence of a recent gas accretion (“rejuvenation”) event, which is fueling low levels of star and cluster formation (Section 8).
3. There is a strong linear correlation between a galaxy’s offset from the MS and the fraction of its cluster population in the MAP. In contrast to the YCL, dust is not a confounding factor as the width of the MAP indicates low amounts of reddening. Above the MS, the presence of a strong MAP feature indicates the elevated star and cluster formation activity must have a duration on the order of 100 Myr. Below the MS, galaxies appear to have a deficient MAP feature, which is consistent with a two-component disk model where flocculent patterns arise through gravitational instabilities in a low-mass cool disk component embedded in a massive halo, which has recently accreted gas after a period of quiescence (Section 8.2).

This presentation of the PHANGS-HST star cluster and association catalogs of observed photometric properties provides a foundation for a broad range of science. Previous studies of star formation and feedback timescales, and cluster formation and evolution, which were performed with more limited samples, can now be expanded with this large sample of ∼100,000 star clusters and compact associations to probe the interplay of the small-scale physics of gas and star formation with galactic structure and galaxy evolution. These catalogs are an essential complement for JWST studies of the earliest phases of dust embedded star and cluster formation, and for extending the study of the observed cluster properties into the infrared. In Paper II, we discuss the derivation of cluster masses, ages, and reddenings based on improved SED fitting methods for UV–optical photometry, and present the companion catalog of physical properties.

Acknowledgments

We dedicate this paper to the memory of Julie Whitmore (1954 January 13–2023 August 23).

J.C.L. is enormously grateful to Michele Judd, Janet Seid, and the W.M. Keck Institute for Space Studies (KISS) at Caltech for its sustained support of collaboration meetings where key work for this paper was performed, and for providing a quiet space for J.C.L. to think. The PHANGS-HST survey benefited from early discussions between J.C.L., A.L., and other current PHANGS team members that date back to the 2014 KISS workshop, “Bridging the Gap: Observations and Theory of Star Formation Meet on Large and Small Scales.”

S.D. is supported by funding from the European Research Council (ERC) under the European Union’s Horizon 2020 research and innovation program (grant agreement No. 101018897 CosmicExplorer).

R.C.L. acknowledges support for this work provided by a National Science Foundation (NSF) Astronomy and Astrophysics Postdoctoral Fellowship under award AST-2102625.

M.B. gratefully acknowledges support from the ANID BASAL project FB210003 and from the FONDECYT regular grant 1211000.

This work was supported by the French government through the France 2030 investment plan managed by the National Research Agency (ANR), as part of the Initiative of Excellence of Université Côte d’Azur under reference No. ANR-15-IDEX-01.

K.K. gratefully acknowledges funding from the Deutsche Forschungsgemeinschaft (DFG, German Research Foundation) in the form of an Emmy Noether Research Group (grant No. KR4598/2-1, PI Kreckel) and the European Research Council’s starting grant ERC StG-101077573 (“ISM-METALS”).

Q.T. acknowledges generous support from the Adelphic Educational Fund Wesleyan Summer Grants for a summer internship in Baltimore and thanks the Johns Hopkins University Department of Physics and Astronomy and the Space Telescope Science Institute for hosting him.

K.G. is supported by the Australian Research Council through the Discovery Early Career Researcher Award (DECRA) Fellowship (project No. DE220100766) funded by the Australian Government, and by the Australian Research Council Centre of Excellence for All Sky Astrophysics in 3 Dimensions (ASTRO 3D), through project No. CE170100013.

We thank summer undergraduate intern Lucius Brown (Yale) for his help with artifact identification in the HST images.

This work is based on observations made with the NASA/ESA Hubble Space Telescope, obtained at the Space Telescope Science Institute, which is operated by the Association of Universities for Research in Astronomy, Inc., under NASA contract NAS 5-26555. These observations are associated with program No. 15654.

Software: DOLPHOT (v2.0 Dolphin 2016), CIGALE (Burgarella et al. 2005; Noll et al. 2009; Boquien et al. 2019).

Data Availability

The PHANGS–HST (Ubeda et al. 2021) star cluster catalogs were made publicly available through the Mikulski Archive for Space Telescopes (MAST) in 2024 January: doi:10.17909/jray-9798.

Appendix
Additional Figures

In this section, we show additional figures. Figure 16 presents the correlation plot between host galaxy distances and relative fraction of characteristic regions in color–color diagrams as discussed in Section 5. Figure 17 and the online figure set present the spatial distribution plots discussed in Section 6.

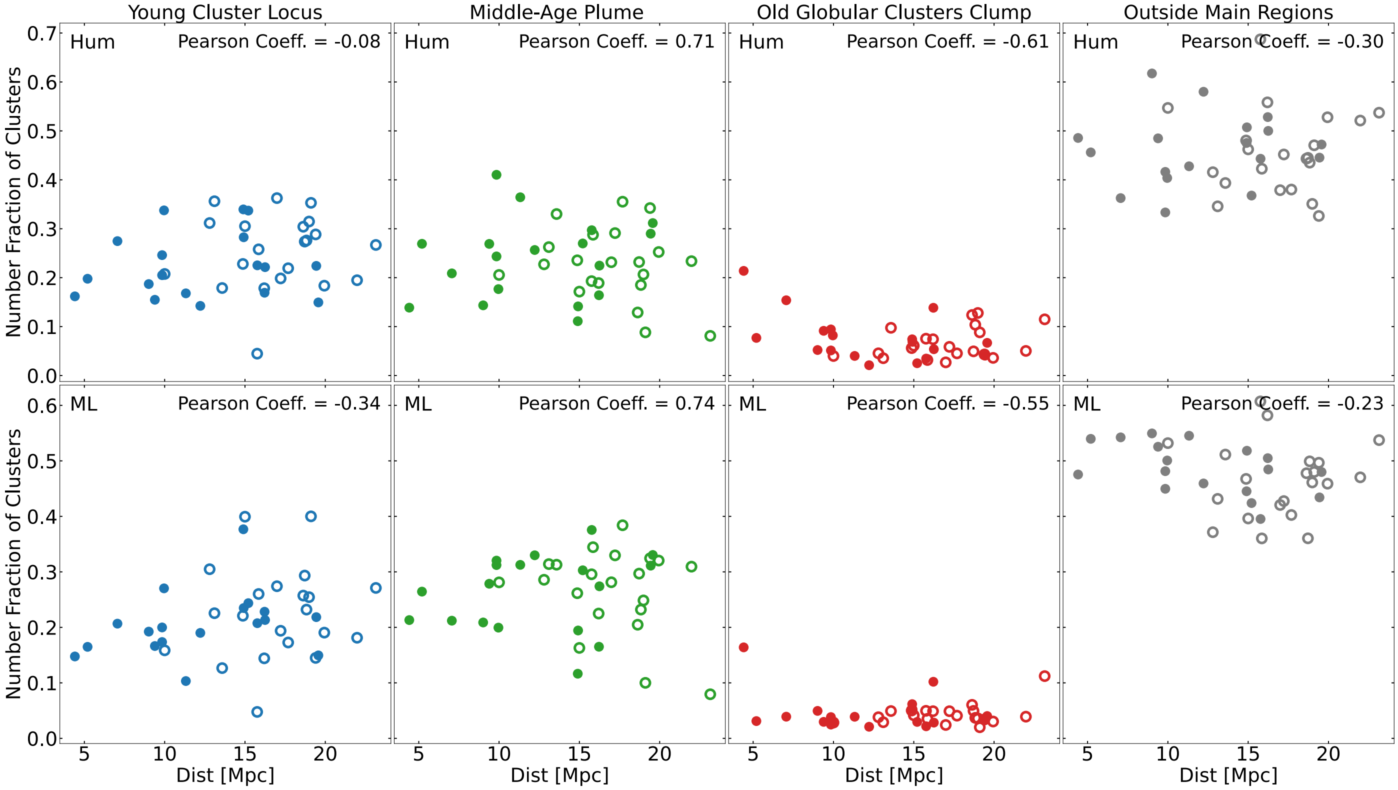

Figure 16. Number fraction of C1 and C2 clusters of each galaxy associated with the main characteristic regions in color–color diagrams found in Section 4.4 as a function of galaxy distance. We show the YCL, the MAP, and the OGC in blue, green, and red, respectively. In gray, we show clusters outside the main regions. We distinguish distance measurements that are estimated from stellar markers such as tip of the red giant branch or from Cepheid variable stars, marked with full circles, whereas other distant measurements are less precise and are marked by empty circles. A complete discussion on each individual distance measurement is provided in Anand et al. (2020) and Anand et al. (2021). For each panel, we show the Pearson correlation coefficient in the top right.

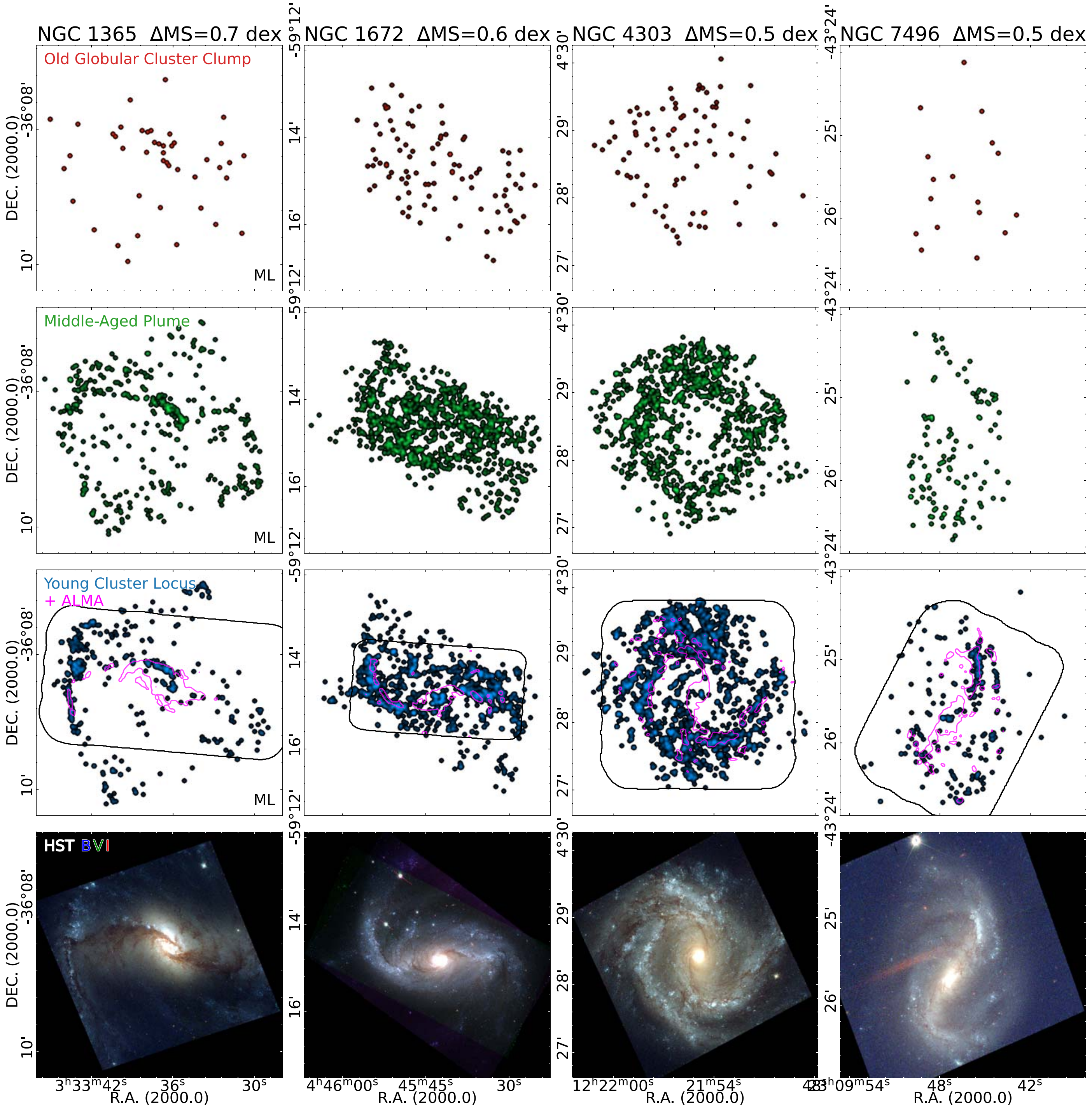

Figure 17. Spatial distributions for ML-classified star clusters of class 1 and 2 as categorized (Section 4.4) into three groups: OGC (red, top panels), MAP (green, upper middle panels), and YCL (blue, lower middle panels); plus color-composite images created from the HST *U*-*B*-*V* bands (bottom panels). The cluster spatial distribution maps are produced by binning the cluster positions onto a pixel grid, which is subsequently convolved with a Gaussian and normalized to unity. In order to highlight the relation between young clusters and molecular gas, with magenta lines, we overlay the ALMA CO(2-1) intensity contours of the 95 percentile on the YCL distribution maps. In this figure and the online figure set, we show the spatial cluster distribution for all PHANGS–HST galaxies sorted by decreasing ΔMS values (see Figure 13).

(The complete figure set (10 images) is available.)

ORCID iDs

Daniel Maschmann https://orcid.org/0000-0001-6038-9511
Janice C. Lee https://orcid.org/0000-0002-2278-9407
David A. Thilker https://orcid.org/0000-0002-8528-7340
Bradley C. Whitmore https://orcid.org/0000-0002-3784-7032
Sinan Deger https://orcid.org/0000-0003-1943-723X
Médéric Boquien https://orcid.org/0000-0003-0946-6176
Rupali Chandar https://orcid.org/0000-0003-0085-4623
Daniel A. Dale https://orcid.org/0000-0002-5782-9093
Aida Wofford https://orcid.org/0000-0001-8289-3428
Kirsten L. Larson https://orcid.org/0000-0003-3917-6460
Adam K. Leroy https://orcid.org/0000-0002-2545-1700

Eva Schinnerer https://orcid.org/0000-0002-3933-7677
Erik Rosolowsky https://orcid.org/0000-0002-5204-2259
Leonardo Úbeda https://orcid.org/0000-0001-7130-2880
Ashley T. Barnes https://orcid.org/0000-0003-0410-4504
Eric Emsellem https://orcid.org/0000-0002-6155-7166
Brent Groves https://orcid.org/0000-0002-9768-0246
Rémy Indebetouw https://orcid.org/0000-0002-4663-6827
Hwihyun Kim https://orcid.org/0000-0003-4770-688X
Ralf S. Klessen https://orcid.org/0000-0002-0560-3172
Kathryn Kreckel https://orcid.org/0000-0001-6551-3091
Rebecca C. Levy https://orcid.org/0000-0003-2508-2586
Francesca Pinna https://orcid.org/0000-0001-5965-3530
M. Jimena Rodríguez https://orcid.org/0000-0002-0579-6613
Qiushi Tian https://orcid.org/0009-0009-9148-2159
Thomas G. Williams https://orcid.org/0000-0002-0012-2142

References

Adamo, A., Ryon, J. E., Messa, M., et al. 2017, ApJ, 841, 131
Adamo, A., Zeidler, P., Kruijssen, J. M. D., et al. 2020, SSRv, 216, 69
Anand, G., Lee, J., van Dyk, S., et al. 2020, AAS Meeting, 236, 336.01
Anand, G. S., Lee, J. C., Van Dyk, S. D., et al. 2021, MNRAS, 501, 3621
Arp, H., & Sulentic, J. W. 1991, ApJ, 375, 569
Athanassoula, E. 1992, MNRAS, 259, 345
Barnes, A. T., Chandar, R., Kreckel, K., et al. 2022, A&A, 662, L6
Barnes, A. T., Watkins, E. J., Meidt, S. E., et al. 2023, ApJL, 944, L22
Bastian, N., Adamo, A., Gieles, M., et al. 2012, MNRAS, 419, 2606
Beuther, H., Meidt, S., Schinnerer, E., Paladino, R., & Leroy, A. 2017, A&A, 597, A85
Boquien, M., Burgarella, D., Roehlly, Y., et al. 2019, A&A, 622, A103
Boselli, A., Cuillandre, J. C., Fossati, M., et al. 2016, A&A, 587, A68
Bradley, L. 2023, astropy/photutils: v1.8.0, Zenodo, doi:10.5281/ZENODO.7946442
Brandt, W. N., Halpern, J. P., & Iwasawa, K. 1996, MNRAS, 281, 687
Brodie, J. P., & Strader, J. 2006, ARA&A, 44, 193
Brown, G., & Gnedin, O. Y. 2021, MNRAS, 508, 5935
Bruzual, G., & Charlot, S. 2003, MNRAS, 344, 1000
Burgarella, D., Buat, V., & Iglesias-Páramo, J. 2005, MNRAS, 360, 1413
Buta, R. J., Sheth, K., Athanassoula, E., et al. 2015, ApJS, 217, 32
Calzetti, D., Lee, J. C., Sabbi, E., et al. 2015, AJ, 149, 51
Cardelli, J. A., Clayton, G. C., & Mathis, J. S. 1989, ApJ, 345, 245
Catinella, B., Saintonge, A., Janowiecki, S., et al. 2018, MNRAS, 476, 875
Chandar, R., Whitmore, B. C., Calzetti, D., & O'Connell, R. 2014, ApJ, 787, 17
Chandar, R., Whitmore, B. C., Kim, H., et al. 2010, ApJ, 719, 966
Choksi, N., & Gnedin, O. Y. 2019, MNRAS, 488, 5409
Cook, D. O., Lee, J. C., Adamo, A., et al. 2019, MNRAS, 484, 4897
Cook, D. O., Lee, J. C., Adamo, A., et al. 2023, MNRAS, 519, 3749
Costa, A. H., Johnson, K. E., Indebetouw, R., et al. 2021, ApJ, 918, 76
Crowl, H. H., & Kenney, J. D. P. 2008, AJ, 136, 1623
Cuevas-Otahola, B., Mayya, Y. D., Arriaga-Hernández, J., Puerari, I., & Bruzual, G. 2023, MNRAS, 525, 5262
de Meulenaer, P., Narbutis, D., Mineikis, T., & Vansevičius, V. 2013, A&A, 550, A20
Deger, S., Lee, J. C., Whitmore, B. C., et al. 2022, MNRAS, 510, 32
Dobbs, C. L., & Pringle, J. E. 2010, MNRAS, 409, 396
Dolphin, A., 2016 DOLPHOT: Stellar photometry, Astrophysics Source Code Library, ascl:1608.013
Egorov, O. V., Kreckel, K., Glover, S. C. O., et al. 2023, A&A, 678, A153
Elmegreen, B. G., & Thomasson, M. 1993, A&A, 272, 37
Elmegreen, D. M., & Elmegreen, B. G. 1987, ApJ, 314, 3
Elmegreen, D. M., Elmegreen, B. G., Frogel, J. A., et al. 2002, AJ, 124, 777
Emig, K. L., Bolatto, A. D., Leroy, A. K., et al. 2020, ApJ, 903, 50
Emsellem, E., Schinnerer, E., Santoro, F., et al. 2022, A&A, 659, A191
Fall, S. M., & Chandar, R. 2012, ApJ, 752, 96
Floyd, M., Chandar, R., Whitmore, B. C., et al. 2024, AJ, 167, 95
Fouesneau, M., & Lançon, A. 2010, A&A, 521, A22
Fouesneau, M., Lançon, A., Chandar, R., & Whitmore, B. C. 2012, ApJ, 750, 60
Gieles, M., & Portegies Zwart, S. F. 2011, MNRAS, 410, L6
Girardi, L., Chiosi, C., Bertelli, G., & Bressan, A. 1995, A&A, 298, 87
Gouliermis, D. A., Hony, S., & Klessen, R. S. 2014, MNRAS, 439, 3775
Grasha, K., Calzetti, D., Adamo, A., et al. 2015, ApJ, 815, 93
Grasha, K., Calzetti, D., Adamo, A., et al. 2017, ApJ, 840, 113
Grasha, K., Calzetti, D., Adamo, A., et al. 2019, MNRAS, 483, 4707
Groves, B., Kreckel, K., Santoro, F., et al. 2023, MNRAS, 520, 4902
Hannon, S., Whitmore, B. C., Lee, J. C., et al. 2023, MNRAS, 526, 2991
Hassani, H., Rosolowsky, E., Koch, E. W., et al. 2024, ApJS, 271, 2
He, K., Zhang, X., Ren, S., & Sun, J. 2015, arXiv:1512.03385
Hogg, D. E., Roberts, M. S., Bregman, J. N., & Haynes, M. P. 2001, AJ, 121, 1336
Hollyhead, K., Bastian, N., Adamo, A., et al. 2015, MNRAS, 449, 1106
Johnson, K. E., Leroy, A. K., Indebetouw, R., et al. 2015, ApJ, 806, 35
Kenney, J. D., & Young, J. S. 1986, ApJL, 301, L13
Kennicutt, R. C., & Evans, N. J. 2012, ARA&A, 50, 531
Kennicutt, R. C., Jr. 1983, AJ, 88, 483
Krumholz, M. R., Adamo, A., Fumagalli, M., et al. 2015, ApJ, 812, 147
Krumholz, M. R., McKee, C. F., & Bland-Hawthorn, J. 2019, ARA&A, 57, 227
Kuno, N., Sato, N., Nakanishi, H., et al. 2007, PASJ, 59, 117
Lada, C. J., & Lada, E. A. 2003, ARA&A, 41, 57
Lang, P., Meidt, S. E., Rosolowsky, E., et al. 2020, ApJ, 897, 122
Larsen, S. S., & Richtler, T. 1999, A&A, 345, 59
Larson, K. L., Lee, J. C., Thilker, D. A., et al. 2023, MNRAS, 523, 6061
Lee, J. C., Gil de Paz, A., Tremonti, C., et al. 2009, ApJ, 706, 599
Lee, J. C., Kennicutt, R. C., & Funes 2007, ApJL, 671, L113
Lee, J. C., Sandstrom, K. M., Leroy, A. K., et al. 2023, ApJL, 944, L17
Lee, J. C., Whitmore, B. C., Thilker, D. A., et al. 2022, ApJS, 258, 10
Leroy, A. K., Sandstrom, K. M., Lang, D., et al. 2019, ApJS, 244, 24
Leroy, A. K., Schinnerer, E., Hughes, A., et al. 2021, ApJS, 257, 43
Levy, R. C., Bolatto, A. D., Leroy, A. K., et al. 2021, ApJ, 912, 4
Levy, R. C., Bolatto, A. D., Leroy, A. K., et al. 2022, ApJ, 935, 19
Linden, S. T., Evans, A. S., Armus, L., et al. 2023, ApJL, 944, L55
Linden, S. T., Evans, A. S., Larson, K., et al. 2021, ApJ, 923, 278
Linden, S. T., Perez, G., Calzetti, D., et al. 2022, ApJ, 935, 166
Maraston, C. 1998, MNRAS, 300, 872
Mayya, Y. D., Romano, R., Rodríguez-Merino, L. H., et al. 2008, ApJ, 679, 404
Messa, M., Adamo, A., Östlin, G., et al. 2018, MNRAS, 473, 996
Moustakas, J., Kennicutt, R. C. J., Tremonti, C. A., et al. 2010, ApJS, 190, 233
Nguyen Luong, Q., Motte, F., Schuller, F., et al. 2011, A&A, 529, A41
Noeske, K. G., Weiner, B. J., Faber, S. M., et al. 2007, ApJL, 660, L43
Noll, S., Burgarella, D., Giovannoli, E., et al. 2009, A&A, 507, 1793
Orozco-Duarte, R., Wofford, A., Vidal-García, A., et al. 2022, MNRAS, 509, 522
Peng, Y.-j., Lilly, S. J., Kovač, K., et al. 2010, ApJ, 721, 193
Pérez, G., Messa, M., Calzetti, D., et al. 2021, ApJ, 907, 100
Popescu, B., Hanson, M. M., & Elmegreen, B. G. 2012, ApJ, 751, 122
Portegies Zwart, S. F., McMillan, S. L. W., & Gieles, M. 2010, ARA&A, 48, 431
Querejeta, M., Schinnerer, E., Meidt, S., et al. 2021, A&A, 656, A133
Renaud, F. 2018, NewAR, 81, 1
Rico-Villas, F., Martín-Pintado, J., González-Alfonso, E., Martín, S., & Rivilla, V. M. 2020, MNRAS, 491, 4573
Rodríguez, M. J., Lee, J. C., Whitmore, B. C., et al. 2023, ApJL, 944, L26
Ryon, J. E., Gallagher, J. S., Smith, L. J., et al. 2017, ApJ, 841, 92
Salim, S., Lee, J. C., Janowiecki, S., et al. 2016, ApJS, 227, 2
Salim, S., Rich, R. M., Charlot, S., et al. 2007, ApJS, 173, 267
Scheuermann, F., Kreckel, K., Barnes, A. T., et al. 2023, MNRAS, 522, 2369
Schinnerer, E., Emsellem, E., Henshaw, J. D., et al. 2023, ApJL, 944, L15
Schinnerer, E., Leroy, A., Blanc, G., et al. 2019, Msngr, 177, 36
Searle, L., Wilkinson, A., & Bagnuolo, W. G. 1980, ApJ, 239, 803
Sellwood, J. A., & Masters, K. L. 2022, ARA&A, 60, 73
Sellwood, J. A., & Wilkinson, A. 1993, RPPh, 56, 173
Silva-Villa, E., & Larsen, S. S. 2011, A&A, 529, A25
Simonyan, K., & Zisserman, A. 2015, arXiv:1409.1556
Skillman, E. D., Kennicutt, R. C., Jr., Shields, G. A., & Zaritsky, D. 1996, ApJ, 462, 147
Smith, L. J., Bastian, N., Konstantopoulos, I. S., et al. 2007, ApJL, 667, L145
Sormani, M. C., Barnes, A. T., Sun, J., et al. 2023, MNRAS, 523, 2918
Sormani, M. C., Tress, R. G., Glover, S. C. O., et al. 2020, MNRAS, 497, 5024
Stetson, P. B. 1987, PASP, 99, 191
Sun, J., He, H., Batschkun, K., et al. 2024, ApJ, 967, 133
Tang, J., Grasha, K., & Krumholz, M. R. 2023, arXiv:2301.05912
Thilker, D., Lee, J., Whitmore, B., et al. 2024, ApJ, submitted
Thilker, D. A., Lee, J. C., Deger, S., et al. 2023, ApJL, 944, L13
Thilker, D. A., Whitmore, B. C., Lee, J. C., et al. 2022, MNRAS, 509, 4094
Tress, R. G., Sormani, M. C., Glover, S. C. O., et al. 2020, MNRAS, 499, 4455
Turner, J. A., Dale, D. A., Lee, J. C., et al. 2021, MNRAS, 502, 1366
Turner, J. A., Dale, D. A., Lilly, J., et al. 2022, MNRAS, 516, 4612

Ubeda, L., Whitmore, B., Thilker, D., et al. 2021, Physics at High Angular resolution in Nearby GalaxieS—HST ("PHANGS-HST"), STScI/MAST, doi:10.17909/T9-R08F-DQ31
van den Bergh, S., & Hagen, G. L. 1968, AJ, 73, 569
Vázquez, G. A., & Leitherer, C. 2005, ApJ, 621, 695
Vollmer, B., Balkowski, C., Cayatte, V., van Driel, W., & Huchtmeier, W. 2004, A&A, 419, 35
Ward, J. L., & Kruijssen, J. M. D. 2018, MNRAS, 475, 5659
Ward, J. L., Kruijssen, J. M. D., & Rix, H.-W. 2020, MNRAS, 495, 663
Watkins, E. J., Barnes, A. T., Henny, K., et al. 2023a, ApJL, 944, L24
Watkins, E. J., Kreckel, K., Groves, B., et al. 2023b, A&A, 676, A67
Wei, W., Huerta, E. A., Whitmore, B. C., et al. 2020, MNRAS, 493, 3178
Whitmore, B. C., Chandar, R., Lee, J. C., et al. 2023a, MNRAS, 520, 63
Whitmore, B. C., Chandar, R., Rodríguez, M. J., et al. 2023b, ApJL, 944, L14
Whitmore, B. C., Chandar, R., Schweizer, F., et al. 2010, AJ, 140, 75
Whitmore, B. C., Lee, J. C., Chandar, R., et al. 2021, MNRAS, 506, 5294
Williams, T. G., Lee, J. C., Larson, K. L., et al. 2024, ApJS, 273, 13
Wofford, A., Charlot, S., Bruzual, G., et al. 2016, MNRAS, 457, 4296
Wright, N. J. 2020, NewAR, 90, 101549
Zaritsky, D., Kennicutt, R. C. J., & Huchra, J. P. 1994, ApJ, 420, 87